

Impact of soil moisture and convectively generated waves on the initiation of a West African mesoscale convective system

C. E. Birch,^{a*} D. J. Parker,^a A. O’Leary,^a J. H. Marsham,^b C. M. Taylor,^c P. P. Harris^c and G. M. S. Lister^d

^a*Institute for Climate and Atmospheric Science, School of Earth and Environment, University of Leeds, UK*

^b*National Centre for Atmospheric Science (NCAS), School of Earth and Environment, University of Leeds, UK*

^c*Centre for Ecology and Hydrology, Wallingford, UK*

^d*NCAS Computer Modelling Services, Department of Meteorology, University of Reading, UK*

*Correspondence to: C. E. Birch, Institute for Climate and Atmospheric Science, School of Earth and Environment, University of Leeds, Leeds, LS2 9JT, UK. E-mail: C.E.Birch@leeds.ac.uk

A mesoscale convective system (MCS) case study was observed over northeast Mali as part of the African Monsoon Multidisciplinary Analysis (AMMA) on 31 July 2006. Observations of this case suggest that the soil-moisture heterogeneity and atmospheric gravity waves emitted from a ‘parent’ MCS were important trigger mechanisms for this system. This study uses high-resolution Met Office Unified Model (MetUM) simulations to assess the importance of the synoptic circulation, land-surface and gravity waves in the initiation and development of the MCS. During the early afternoon shallow convection developed over a region of dry soil within a synoptic-scale convergence zone, which was caused by the confluence of the southerly monsoon flow with winds associated with the circulation around the Saharan heat low. Two pronounced waves were emitted from a nearby ‘parent’ storm and propagated towards the convergence zone. When the second wave reached the location of the shallow convection, deep convection was immediately initiated. Further convective cells developed later in the afternoon over dry soil, many adjacent to strong soil moisture gradients; these aggregated with the main storm, which later developed into the case study MCS. A comparison of model simulations with/without the soil-moisture heterogeneity and gravity waves shows that the synoptic-scale circulation and convergence zones, specified by the atmospheric analysis, were the most important factors for the successful simulation of the MCS. If the location of the initiation of the system is to be forecast accurately, the land-surface, that is, the soil moisture, must be represented adequately. In order to reproduce the timing of the secondary initiation of convection correctly the model must be able to capture gravity waves that are emitted by existing systems.

Key Words: mesoscale convective system (MCS); secondary initiation; gravity wave; soil moisture; AMMA

Received 17 April 2012; Revised 11 September 2012; Accepted 27 September 2012; Published online in Wiley Online Library 20 December 2012

Citation: Birch CE, Parker DJ, O’Leary A, Marsham JH, Taylor CM, Harris P, Lister G. 2013. Impact of soil moisture and convectively generated waves on the initiation of a West African mesoscale convective system. *Q. J. R. Meteorol. Soc.* **139**: 1712–1730. DOI:10.1002/qj.2062

1. Introduction

1.1. Convection and land-surface interaction over West Africa

The Sahel region of West Africa receives 80–90% of its annual rainfall through convective clouds, mainly in the form of mesoscale convective systems (MCSs) (Laurent *et al.*, 1998; Mathon *et al.*, 2002). The Sahel has suffered serious droughts during recent decades (Janicot *et al.*, 2008) and therefore it is important that rainfall variability can be predicted on various time-scales. There are currently problems with rainfall prediction over West Africa, both at numerical weather prediction (Meynadier *et al.*, 2010; Agustí-Panareda *et al.*, 2010c) and at climate scales (Hourdin *et al.*, 2010). MCSs are a particular problem in global models because accurate representation of their trajectories, propagation speed and precipitation distribution requires the explicit treatment of moist convection.

Taylor *et al.* (1997) and Koster *et al.* (2004) show that in semi-arid regions such as West Africa, soil moisture has a strong influence on precipitation. Moist convection requires both a humidity and heat source. Compared with dry soil, the boundary layer is cooler and moister over wet patches (Kohler *et al.*, 2010). In a one-dimensional framework, fluxes of equivalent potential temperature are almost independent of Bowen ratio (as discussed by Garcia-Carreras, 2011) and it is therefore unclear, *a priori*, whether new convection will form over hot, dry or wet, cool surfaces. Observations have shown that new convective cells generally initiate preferentially over surfaces with locally enhanced sensible heat fluxes, that is, over warm, dry soil (Carleton *et al.*, 2001; Negri *et al.*, 2004; Taylor and Ellis, 2006; Wang *et al.*, 2009); in the case of soil moisture, this implies a negative soil moisture–precipitation feedback. One reason for this is that although over wet soils the lower sensible heat fluxes reduce entrainment of low equivalent potential temperature air, which increases convective available potential energy (CAPE), the shallower convective boundary layer (CBL) with a strong lid tends to lead to higher convective inhibition (CIN; Adler *et al.*, 2011; Garcia-Carreras *et al.*, 2011). Soil moisture heterogeneity can cause horizontal gradients in near-surface temperature, which can generate mesoscale circulations analogous to a land-sea breeze (Segal and Arritt, 1992). These circulations can cause moisture convergence and a minimum in the entrainment–dilution of CBL air (Taylor *et al.*, 2007; Adler *et al.*, 2011; Garcia-Carreras *et al.*, 2011), favouring deep convection during the afternoon (Emori, 1998). For these reasons, the optimum location for convection initiation appears to be on dry soil that is adjacent to strong gradients in soil moisture (Taylor *et al.*, 2011).

Although the soil moisture–precipitation feedback appears to be negative in the early stages of convection, when the system is in its mature stage the feedback can be positive (Gantner and Kalthoff, 2010). Taylor and Lebel (1998) use a dense network of rain-gauges to show a strong preference for increased rainfall at stations where it had rained in the previous 2–3 days. Similarly, Wolters *et al.* (2010) show, using a mesoscale weather model, that precipitation intensity is greater over wet soil. Convective systems become more intense over wet soil due to the increased availability of moisture and CAPE at the surface (Taylor and Clark, 2001; Gantner and Kalthoff, 2010).

Representation of the soil moisture–precipitation feedback in models is uncertain (Gaertner *et al.*, 2010) because soil moisture is not well represented (Agustí-Panareda *et al.*, 2010a, 2010b) and there are large biases in the water budget (Meynadier, 2010). Soil moisture is also not the only precipitation trigger mechanism. Klüpfel *et al.* (2011a) used high-resolution simulations to assess the impact of a number of soil-moisture fields on precipitation in the Sahel and Sudan regions. They concluded that although there were major variations in the precipitation produced in the simulations, the timing of convection initiation was influenced mainly by the atmospheric forcing. A similar result was found by Guichard *et al.* (2010), who found that the conditions used to initialize both mesoscale and global models had a significant control on the location of rainfall at synoptic scales.

1.2. Secondary initiation of storms

There are three possible mechanisms for the secondary initiation of convection over West Africa: (i) dynamical lifting by cold pools; (ii) waves in the form of a bore or solitary wave, which are induced by the cold pool; and (iii) waves that are generated by the updrafts within a convective system and propagate horizontally in a waveguide. Storm outflows, caused by evaporatively cooled downdrafts, are analogous to gravity currents (Charba, 1974; Mueller and Carbone, 1987). Cold air slumps downwards to the surface in the storm and then spreads out radially. The gust front (leading edge of the cold pool) is marked by a region of low-level convergence and ascent (Charba, 1974; Goff, 1976). These fronts can trigger deep convection by dynamically forcing the top of the boundary layer to ascend (Emanuel, 1994; Xue *et al.*, 1997; Lin *et al.*, 1998; Lothon *et al.*, 2011) or by the collision of two mature cold pools (Droegemeier and Wilhelmson, 1985a, 1985b; Tompkins, 2001).

Gravity currents can generate a bore or solitary wave in front of the current head, which propagates along interfaces between fluids of different densities (e.g. Crook and Miller, 1985; Rottman and Simpson, 1989; Knupp, 2006). Such waves have been observed to propagate on the surface nocturnal inversion layer in US storm case-studies (Koch *et al.*, 2008), or on the elevated stable layer remaining after the passage of a sea-breeze flow in Australia (Smith, 1988; Goler and Reeder, 2004). Such waves can travel faster than the head of the current and, unlike the cold pool, they are not directly eroded by the heat fluxes at the surface, which means the waves can propagate much further in the horizontal than the gravity current (Ross *et al.* (2004) describe the erosion of gravity currents in this way). However, there is currently no clear evidence of daytime solitary waves in the Sahelian environment either from observational or model studies.

Cloud systems or MCSs generate waves that can either enhance or suppress further convection in the region surrounding the ‘parent’ storm (Mapes, 1993; Liu and Moncrieff, 2004). Tropospheric gravity waves emitted from mid-latitude MCSs and their impact on convection triggering and organization is reasonably well documented (e.g. Raymond, 1983; Uccellini and Koch, 1987; Stobie *et al.*, 1983; Marsham and Parker, 2006). Over the Tropics deep convection is at a maximum (Pfister *et al.*, 1993) and the influence of the resulting gravity waves is larger due to the reduced effect of the Coriolis force (Liu and Moncrieff, 2004). Stensrud and Fritsch (1993, 1994) and

Anabor *et al.* (2009) suggest that it is the combined effect of internal gravity waves and cold pools that control the upstream propagation of MCS events. Gravity waves lead to the initial upstream development of convection, but once it is established and cold pools begin to form, it is the cold pools that dominate the subsequent convective development.

The majority of the previous work on secondary initiation has been performed using idealized, cloud-resolving simulations (e.g Lane and Reeder, 2001; Beres *et al.*, 2002; Song *et al.*, 2003; Lane and Zhang, 2011). There have been only a handful of observed cases that have been studied in an atmospheric model (Piani *et al.*, 2000; Lac *et al.*, 2002; Morcrette *et al.*, 2006; Marsham and Parker, 2006). None of these cases were over West Africa. Bretherton and Smolarkiewicz (1989) show that linear tropospheric gravity waves propagate radially from convective clouds, providing compensating subsidence for the updrafts within the cloud system. Mapes (1993) applied this idea to MCSs in the tropics, where wind shear is weak for much of the time. He showed that a prescribed heat source (such as an MCS) can generate horizontally propagating wave-fronts, which have vertical wavelengths that are harmonics of the depth of the waveguide. The $n = 1$ wave mode has a vertical wavelength equal to twice the depth of the waveguide; it travels fast and induces deep subsidence. The $n = 2$ and $n = 3$ wave modes can induce ascent in the lower troposphere, which produces favourable conditions for new convection.

1.3. Case study background

Observations of the mesoscale convective system used in this case study are described in detail by Taylor *et al.* (2010). They describe the initiation and development of the storm using *in situ* aircraft, dropsonde and satellite observations made during the AMMA (African Monsoon Multi-disciplinary Analysis) field campaign (Redelsperger *et al.*, 2006). The storm initiated in northeast Mali at approximately 1300 UTC, 31 July 2006 and propagated westwards, until it decayed off the west coast of Africa on 2 August.

Taylor *et al.* (2010) describe two important factors for the initiation and development of the system: (i) the distribution of wet and dry soil in the region of the initiation; and (ii) the influence of an atmospheric wave, emitted by a mature ‘parent’ storm (marked ‘P’ on Figure 1) that was situated ~ 250 km to the south. The case study (‘daughter’) storm initiated at 16.5°N , 1°E over an area of dry soil (marked ‘D’ on Figure 1) that was within a wetter region created by the passage of a MCS on the previous day (30 July 2006). The initiation point was adjacent to a strong soil moisture gradient, upwind of a wet patch. Taylor *et al.* (2010) show that boundary-layer air over the wet patch was cooler than over the dry soil and suggest that this induced a mesoscale circulation similar to a sea breeze, which initiated shallow convection.

Evidence for the atmospheric wave was found in satellite retrievals of brightness temperature, in the form of a band of cloud that was observed to propagate outwards from the parent storm at a speed of $\sim 13 \text{ m s}^{-1}$. This wave reached the daughter storm at approximately 1300 UTC, coinciding with the development of deep convection and high cloud (see green lines in Figure 16). It was not clear from the observations whether the wave took the form of a solitary wave (bore) or a wave-front. The authors suggest that a bore

could propagate along the stable interface between the CBL and the near-neutral Saharan air layer (SAL). Any upward displacement of air caused by the bore could readily generate new convection because, compared with the stratified free-troposphere, the neutrality of the SAL means only a small amount of energy would be needed to produce enough uplift to bring air to its level of free convection. The temperature of the cloud band in the satellite observations did, however, suggest that the observed clouds were at a much higher altitude than the CBL–SAL interface, suggesting that the wave feature was not confined to low-levels and could have taken the form of a wave-front instead.

Klüpfel *et al.* (2011b) used COSMO (Consortium for Small-scale Modeling) simulations at 2.8 km resolution, with explicit deep convection to study the 31 July 2006 MCS case. The simulations suggest that the important triggering mechanisms for the daughter storm were: (i) mesoscale circulations resulting from soil-moisture heterogeneities and (ii) larger scale convergence zones at the initiation location. The parent and daughter storms were reproduced in the simulations, but both appeared approximately 9 h too late and 100–150 km too far south. The model simulations showed that a cyclonic vortex to the northeast caused westerly winds in the CBL over the initiation location on 31 July. During early afternoon precipitating cells formed but did not develop into a larger system because there was no large-scale moisture supply. Later in the day the parent storm moved in from the west, and cooling by the evaporation of rainfall generated a strong density current that propagated northwards. The easterly/southeasterly winds from the cold pool intensified the southerly monsoon flow and converged with the westerly winds associated with the vortex to form a convergence zone north of the parent storm. The reinforced southerly winds also transported moist monsoon air northwards, which reached the daughter initiation location by late evening. At this time deep convection was initiated, which eventually developed into the daughter MCS.

Klüpfel *et al.* (2011b) conclude that the most important triggering mechanism was the low-level synoptic-scale convergence, reinforced by the density current. They do, however, state that the relative importance of the various triggering mechanisms in the simulations is questionable due to the 9 h difference in the initiation time between the observations and model; the mesoscale circulations may have had a greater influence if the modelled storm had initiated during the day, as observed in reality.

The aim of this study is to use high-resolution, convection-permitting model simulations to study the initiation and development of the daughter storm. One of the simulations uses realistic soil moisture patterns, derived from observations, to assess the importance of land-surface variability on the initiation location of the storm. The simulations are also used to characterize the observed atmospheric wave and to determine the importance of waves as a trigger mechanism.

2. Model experiments and set-up

The model simulations were performed using version 7.3 (Parallel Suite 22) of the Met Office Unified Model (MetUM). The MetUM has a semi-Lagrangian, semi-implicit and non-hydrostatic formulation and a terrain-following co-ordinate system (Davies *et al.*, 2005). Many

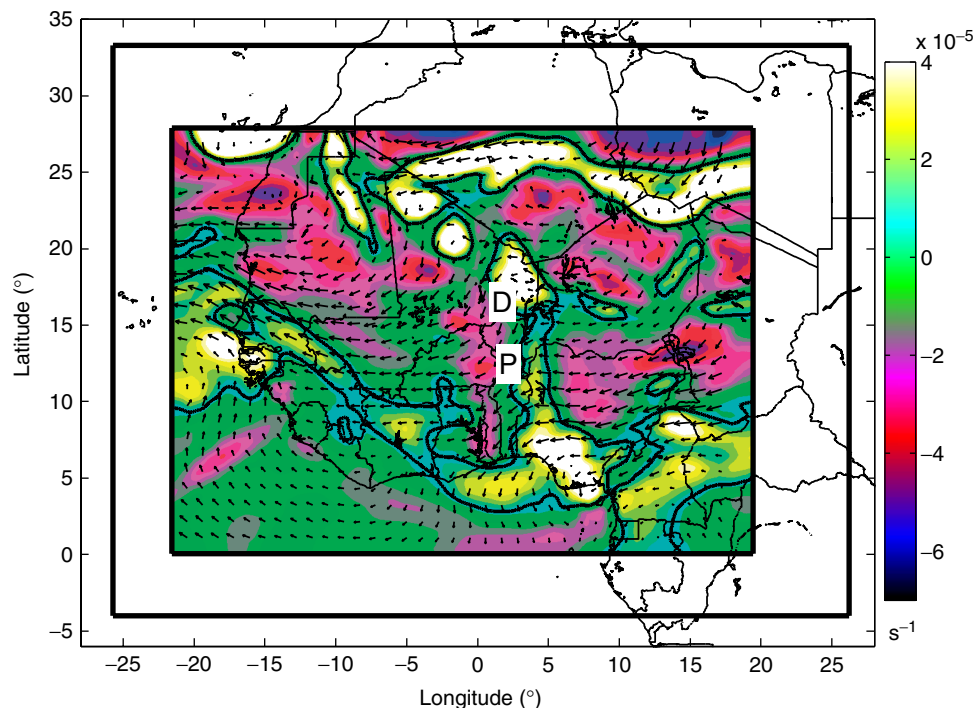


Figure 1. Relative vorticity (shading) and wind vectors at 700 hPa at 1200 UTC, 31 July 2006 from 4 km nest in the control simulation. The thick black lines mark the 10^{-5} s^{-1} relative vorticity contour. The domain sizes of the 4 and 12 km nests are illustrated by the two black boxes. The locations of the daughter and parent storms at 1200 UTC, 31 July 2006 are marked by the 'D' and 'P'. This figure is available in colour online at wileyonlinelibrary.com/journal/qj

types of process are parametrized, such as the surface (Essery *et al.*, 2001), the boundary layer (Lock *et al.*, 2000) and mixed-phase cloud microphysics (Wilson and Ballard, 1999). Convection is parametrized in the global and 12 km nest using the Gregory and Rowntree (1990) scheme and convection is explicit in the 4 km simulations.

The global model was initialized using operational European Centre for Medium-range Weather Forecasts (ECMWF) analyses and is used to create lateral boundary conditions for the 12 km resolution (38 vertical levels) nest. The 12 km nest creates lateral boundary conditions and initial conditions for the 4 km resolution (70 vertical levels) nest. The thick black boxes in Figure 1 show the location and size of the 12 and 4 km domains. Figure 2 illustrates the various model simulations that were performed. The model was initialized at 1200 UTC on both 30 and 31 July 2006 and at 0000 UTC on 30 July 2006 using ECMWF analyses. The best results were obtained using the 1200 UTC, 30 July analysis (see section 3.1 for more details) and this simulation is therefore designated as the 'control'. A restart dump from the 4 km nest was obtained from the control simulation at 0600 UTC on the 31 July 2006. A separate experiment was then initialized with this dump, together with a more realistic soil-moisture distribution ('ASSIM'), and run until 2100 UTC on the 31 July 2006.

The fine horizontal resolution ASSIM soil-moisture field was created by running an off-line simulation of the MetUM's land-surface scheme (Joint UK Land Environment Simulator, JULES; Best *et al.*, 2011), constrained by satellite observations of land-surface temperature (LST) from the EUMETSAT Land SAF (Satellite Applications Facility; Trigo *et al.*, 2008). This JULES simulation was forced with 0.5° near-surface boundary conditions provided by the AMMA Land Surface Model Intercomparison Project, ALMIP (Boone *et al.*, 2009), along with satellite-derived

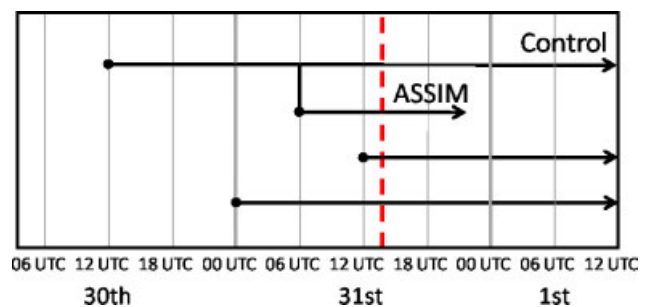


Figure 2. Diagram illustrating the model simulations performed at 4 km horizontal resolution. The dashed line marks the initiation time of the daughter storm. This figure is available in colour online at wileyonlinelibrary.com/journal/qj

0.1° rainfall estimates from EPSAT-SG (Estimation of Precipitation by Satellite – Second Generation; Bergès *et al.*, 2010). The model was constrained daily by adjusting non-zero EPSAT-SG rainfall amounts for each 3 km pixel to give the root-mean-squared best fit between modelled and observed LST, yielding a fine resolution soil moisture estimate on the domain ($10\text{--}20^\circ\text{N}$, $10^\circ\text{W}\text{--}10^\circ\text{E}$) at 0.0275° (~ 3 km) resolution. This model-derived estimate was favoured over the use of a satellite-derived soil moisture product (e.g. from AMSR-E, Advanced Microwave Scanning Radiometer – Earth Observing System) for several reasons: (i) the satellite products provide information on the moisture content of the uppermost soil layer only, whereas JULES computes the moisture on all four of the MetUM's soil levels; (ii) data from AMSR-E are available typically once per day, so new soil-moisture features created after the overpass time are not captured; (iii) AMSR-E soil moisture resolves features on scales of ~ 50 km, but Taylor *et al.* (2011) show that the dominant influence of soil moisture on

convective initiation occurs at finer length scales; and (iv) the modelled surface energy budget is influenced more by the soil moisture content relative to model parameters (the volumetric saturation, critical and wilting points) than by the absolute amount of water in the soil. Regarding this last point, the gridded datasets of these soil parameters that are available for our West African domain are constrained by few observations compared with other regions in the world. They exhibit unrealistic, coarse-scale spatial discontinuities, which, when used in JULES, dominate the spatial variability in the modelled land surface state and fluxes over the variability produced by the fine scale variation in land-cover type and soil moisture. For this reason, the ASSIM soil moisture was computed by JULES using spatially uniform values for these parameters (saturation point = $0.4036 \text{ m}^3 \text{ m}^{-3}$, critical point = $0.2175 \text{ m}^3 \text{ m}^{-3}$ and wilting point = $0.1152 \text{ m}^3 \text{ m}^{-3}$), and the same uniform values were used in the subsequent MetUM simulations. Note that the other soil parameters, such as the soil thermal conductivity and thermal capacity, were also set to constant, relevant values as identified during ALMIP. The ASSIM soil-moisture field was averaged onto the 4 km MetUM grid, smoothed at the boundaries towards the model soil moisture values and merged with the 4 km restart dump. Both the ASSIM soil-moisture field and the MetUM have four soil layers with thicknesses of 0.1 (uppermost), 0.25, 0.65 and 2.0 m.

3. Results

3.1. Evolution of the simulated MCSs

An overview of the synoptic conditions at 1200 UTC, 31 July 2006 is shown in Figure 1. The African Easterly Jet is weak at this time and lies at approximately 11°N . The trough axis of an African Easterly Wave lies at 4°E , between 8 and 20°N . The winds at 700 hPa are predominantly northeasterly over the MCS initiation location, which is marked by the 'D' in Figure 1.

Figure 3 uses 6 h accumulated precipitation from the TRMM3B42 satellite rainfall product (TRMM, Tropical Rainfall Measuring Mission; Huffman *et al.*, 2007) and from the control simulation to give an overview of the initiation and development of the systems. The observations show that an MCS developed on 30 July and produced a large amount of rainfall during the evening of 30 July and early morning of 31 July (black circles in Figure 3(a) and (b)). This system created patches of wet soil in the region 13 – 18°N , 4°W – 3°E . The parent storm initiated on the afternoon of 30 July between 10 – 15°N and 5 – 10°E and tracked westwards until it dissipated during the afternoon of 31 July between 2°W and 2°E (light grey circles in Figure 3(a)–(d)). Even though the details of the model rainfall distribution do not agree well with the observations, the timing, general location and propagation of these two systems are reproduced well by the model (i.e. within 1° and 1 h, Figures 3(g)–(j)).

The daughter MCS storm initiated during the afternoon of 31 July at 16°N , 1°E , developed into a MCS during late afternoon and then propagated towards the west on 1 August (marked by the dark grey circles in Figure 3(d)–(f)). The system reached the west coast of Africa on 2 August and began to dissipate (not shown). Again, the model control simulation reproduces the timing, general location and propagation of this system with good accuracy

(Figure 3(j)–(l)), but the details of the initiation are different to those suggested by the observations.

Hovmöller plots of hourly precipitation rates, averaged between 11 and 18°N , for both the TRMM3B42 and EPSAT-SG (Bergés *et al.*, 2010) satellite products, and the various model simulations are shown in Figure 4. The TRMM3B42 product illustrates the westward propagation of the parent storm (P) between 1200 UTC on 30 July and 1200 UTC on 31 July, followed by the initiation and propagation of the daughter storm (D). The system to the west (WP), which produced the patches of wet soil between 4°W and 3°E is also shown in the satellite precipitation. The EPSAT-SG data have a higher temporal and spatial resolution than the TRMM3B42 data and they are derived from a combination of TRMM data, GPCP-1dd (Global Precipitation Climatology Project) data and multiple channels from the SEVIRI (Spinning Enhanced Visible and Infrared Imager) instrument on the MSG (Meteosat Second Generation) satellite. The propagation of the three systems in the EPSAT-SG product is very similar to that in the TRMM3B42 product, giving confidence in the use of TRMM3B42 data for the comparisons with the model.

Figure 4(c) and (d) show rainfall rates from the control and ASSIM simulations. As shown in Figure 3, the control simulation successfully reproduces the initiation and propagation of the parent and daughter storms. Rainfall from the model simulation that was initialized with an analysis 24 h later (1200 UTC 31 July) than that used in the control simulation is shown in Figure 4(e). The daughter storm is reproduced in this run but the parent storm is absent: the rainfall develops approximately 5 h too late and the system propagates too slowly westwards on 1 August. Figure 4(f) shows rainfall diagnostics from the simulation initialized at 0000 UTC on 31 July. This run is less successful than the runs initialized at 1200 UTC; the rainfall pattern does not resemble the signature of the daughter storm at all.

The reasons for the differences between the simulations are illustrated using plots of 925 hPa potential temperature, specific humidity, winds and convergence at 1200 UTC, on 31 July (Figure 5). In the control simulation and the simulation initialized at 1200 UTC on 31 July the daughter storm develops in a region of synoptic-scale convergence (marked by the black contour lines and the 'D' in Figures 5(a) and 5(b) respectively). This convergence zone forms through the confluence of the moist, southerly winds associated with the parent storm ('P') and the westerly winds associated with the cyclonic circulation around the heat low. The leading edge of the simulated cold pool produced by 'P' is more than 100 km to the southeast of the daughter storm initiation point at 1200 UTC, on 31 July (e.g. see Figure 16 and associated discussion) and therefore cannot directly influence this convergence zone. Klüpfel *et al.* (2011b) conducted a sensitivity simulation of this case, in which the evaporative cooling is removed from their simulation, which suppresses the cold pool from the parent storm. They demonstrate from this that the parent storm does indeed modify the southerly monsoon flow and is a significant factor in the development of this low-level convergence zone, but this is not caused directly by the cold pool.

The synoptic circulation in the simulation initialized at 0000 UTC on 31 July (Figure 5(e) and (f)) is different to the two simulations described above. Neither the parent storm nor the southerly winds north of it are reproduced by the

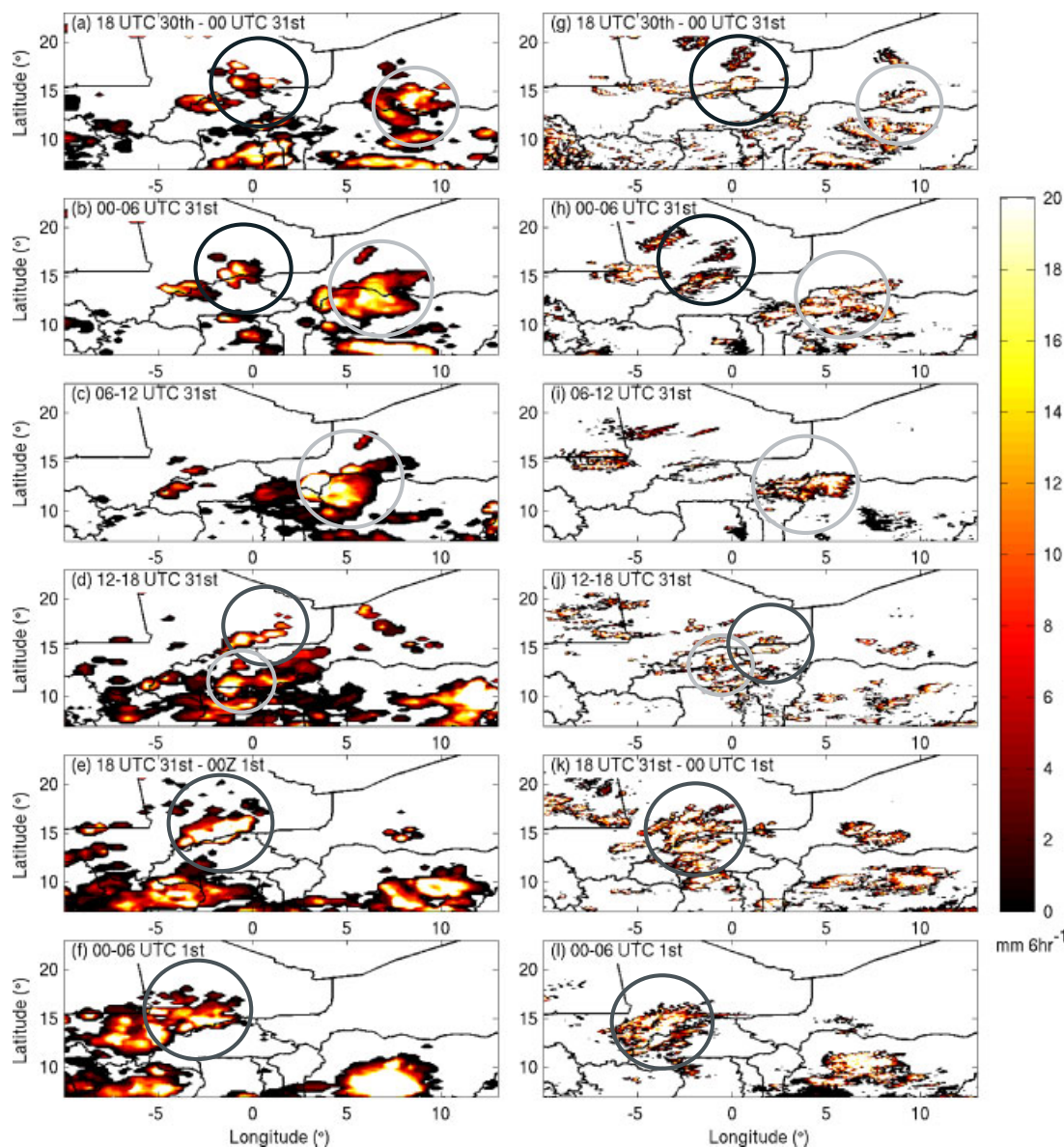


Figure 3. Six-hourly accumulated precipitation ($\text{mm } 6 \text{ h}^{-1}$) from TRMM3B42 ((a)-(f)) and the model control run ((g) and (l)) from 1800 UTC on 30 July 2006 to 0600 UTC on 1 August 2006. The black circles mark the MCS on 30 July that produced the wet soil patches, the light grey circles mark the parent storm and the dark grey circles mark the daughter storm. This figure is available in colour online at wileyonlinelibrary.com/journal/qj

model, and therefore the large-scale convergence zone does not develop. Without this convergence zone the daughter storm is not reproduced (Figure 4(f)).

3.2. Land-atmosphere interaction

In this section the influence of soil moisture on the initiation of the daughter MCS is investigated through a comparison between the control and ASSIM simulations. Figure 6(a) shows soil moisture at 1300 UTC, 31 July 2006, derived from the EPSAT-SG rainfall product and the AMSR-E brightness temperatures (Pellarin *et al.*, 2009). This is produced by estimating soil moisture from a high spatial and temporal resolution rainfall product and then the AMSR-E brightness temperatures are used to account for uncertainties in the rainfall. The satellite product shows mainly wet soil south of 12.5°N , a patch of wet soil in the region $13-18^\circ\text{N}, 3^\circ\text{W}-2^\circ\text{E}$ and drier soil around $16.5^\circ\text{N}, 0.5^\circ\text{W}$ and $13-15^\circ\text{N}, 1-4^\circ\text{E}$. The control run has a distinctive large-scale north-south gradient in soil moisture that originates the ECMWF analysis

(Figure 6(e)); soil moisture decreases between 10 and 13°N , there are very low values between 13 and 17°N and larger values in the northeast of the subdomain, which are associated with a region of slightly elevated orography. The wet patch at $14-16^\circ\text{N}, 5^\circ\text{W}-1.5^\circ\text{E}$ was created by the MCS on the previous day and the wet patch at $11-13^\circ\text{N}, 3-5^\circ\text{E}$ was created by the parent MCS. The ASSIM soil moisture (Figure 6(i)) bears more resemblance to the observations than that in the control run due to the large amount of satellite data used to produce the ASSIM soil-moisture product. The observed north-south gradient and the wet patch centred at $13-18^\circ\text{N}, 3^\circ\text{W}-2^\circ\text{E}$ is reproduced, and like the satellite-derived soil moisture there is a dry patch centred at $14.5^\circ\text{N}, 2^\circ\text{E}$ and a small dry patch surrounded by wet soil at $16.5^\circ\text{N}, 0.5^\circ\text{W}$.

Figure 6(b)-(d) shows MSG brightness temperatures, where white shading depicts cold, high cloud. At 1300 UTC, 31 July 2006 the parent storm is clearly visible in the satellite imagery (marked with a 'P'); it then tracked westwards during the afternoon, reaching 3°W by 1800 UTC. The

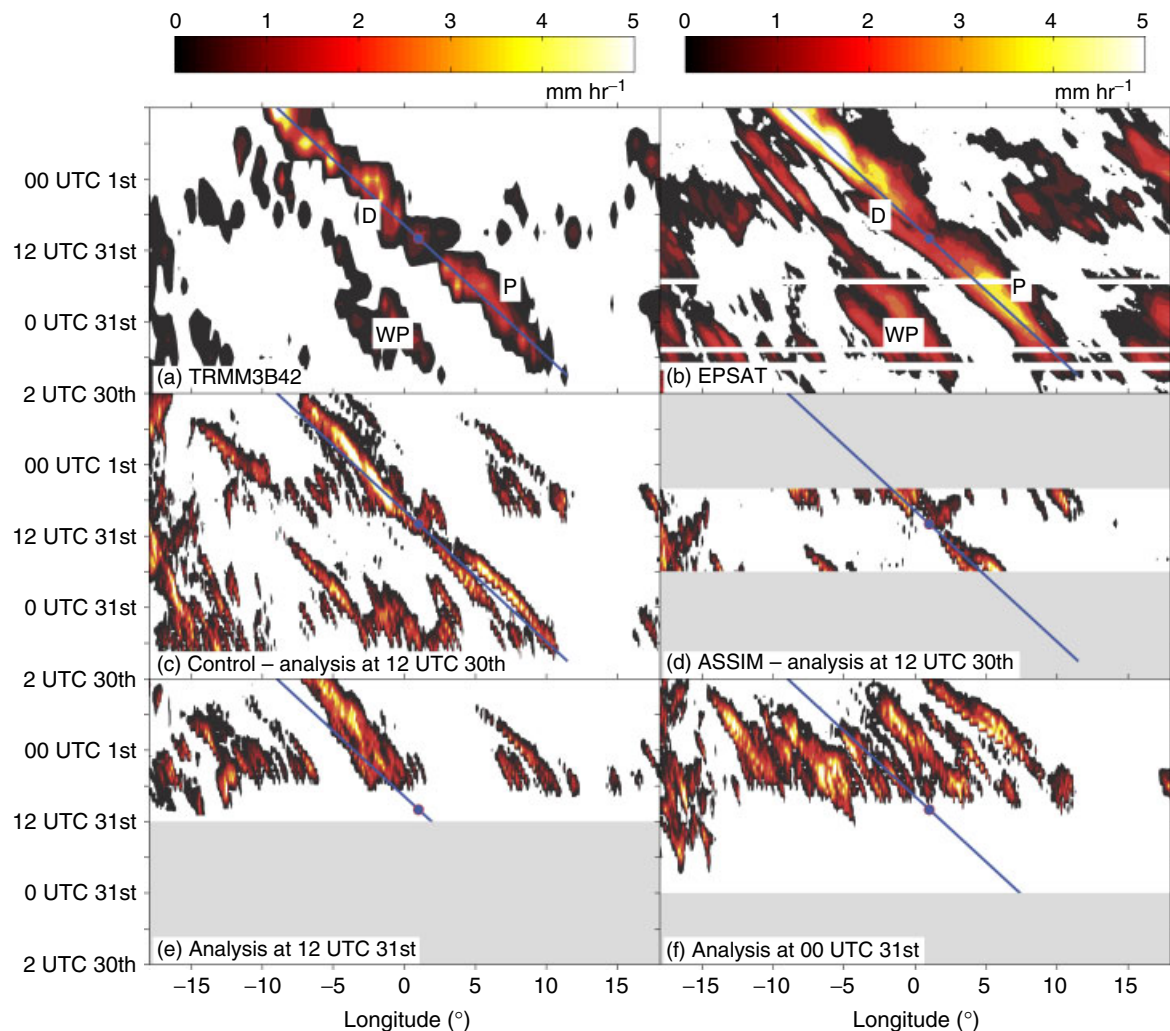


Figure 4. Hovmöller plots of precipitation rate (averaged between 11 and 18°N) for (a) TRMM3B42, (b) EPSAT observations and (c)–(f) various MetUM runs. The diagonal lines mark the track of the parent (P) and daughter (D) storms in the observations, the storm that produced the wet patches on 30 July is marked by ‘WP’ in the observations and the dots mark the commencement of deep convection in the observations. This figure is available in colour online at wileyonlinelibrary.com/journal/qj

location of the daughter storm is illustrated on Figure 6(c) and (d) (marked with a ‘D’); it initiated over relatively dry soil, with a wet patch of soil immediately to the southeast and an additional wet patch approximately 80 km to the northwest (shown in more detail in Figure 3; Taylor *et al.*, 2010). By late afternoon (Figure 6(d)) the daughter storm had increased in size and most of the subsequent convection in the system occurred over wet soil (Taylor *et al.*, 2010).

The position and propagation of the parent storm is similar in the control and ASSIM runs. Between 1300 and 1500 UTC the simulated parent storm is 120–150 km to the east of the observed parent storm and dissipates too early in the afternoon. The daughter storm in both of the model simulations initiates at 1300 UTC over dry soil at 15°N, 1–3°E, approximately 170 km to the southeast of the observed storm. The subsequent evolution of the storm in the model simulations differs to that in the observations. The satellite imagery suggests that the daughter storm initiates at a single point and then develops. In the model simulations the daughter storm grows in size by the accumulation of many individual convective cells, which develop later than the main daughter storm (Figure 6(h) and (l)). These additional cells form on the dry soil but mainly close to the boundaries of the substantial wet patch. The exact location

of these cells differs in the control and ASSIM simulations because the wet patches differ in their position.

The initiation times and locations of the new convective cells in relation to the soil-moisture heterogeneity is shown in more detail in Figure 7. The times were diagnosed subjectively using hourly plots of model rainfall rate. When the rainfall rate associated with a particular cell became continuous over two intervals of 1 h, and prevailed over a region with a radius greater than ~20 km, an initialization time and location was noted on the plot. The preference for initiation over soil-moisture gradients is similar in the two runs, but slightly less widespread in the ASSIM run, which is more consistent with the observations.

In Figure 7 the initiation point of the main daughter storm is marked by ‘14’ at 14.8°N, 2°E in both the control and ASSIM simulations. The location of the parent storm at 1200 UTC is shown on the plots by the thick white contour at 12–14°N, 1–3°E. The daughter storm initiates over a region of dry soil, which is in the same location as the significant boundary-layer convergence caused by the confluence of the moist southerly monsoon winds with the westerly winds to the south of the Saharan heat low.

The differences in boundary-layer structure over the wet and dry soil are illustrated by a tephigram of model

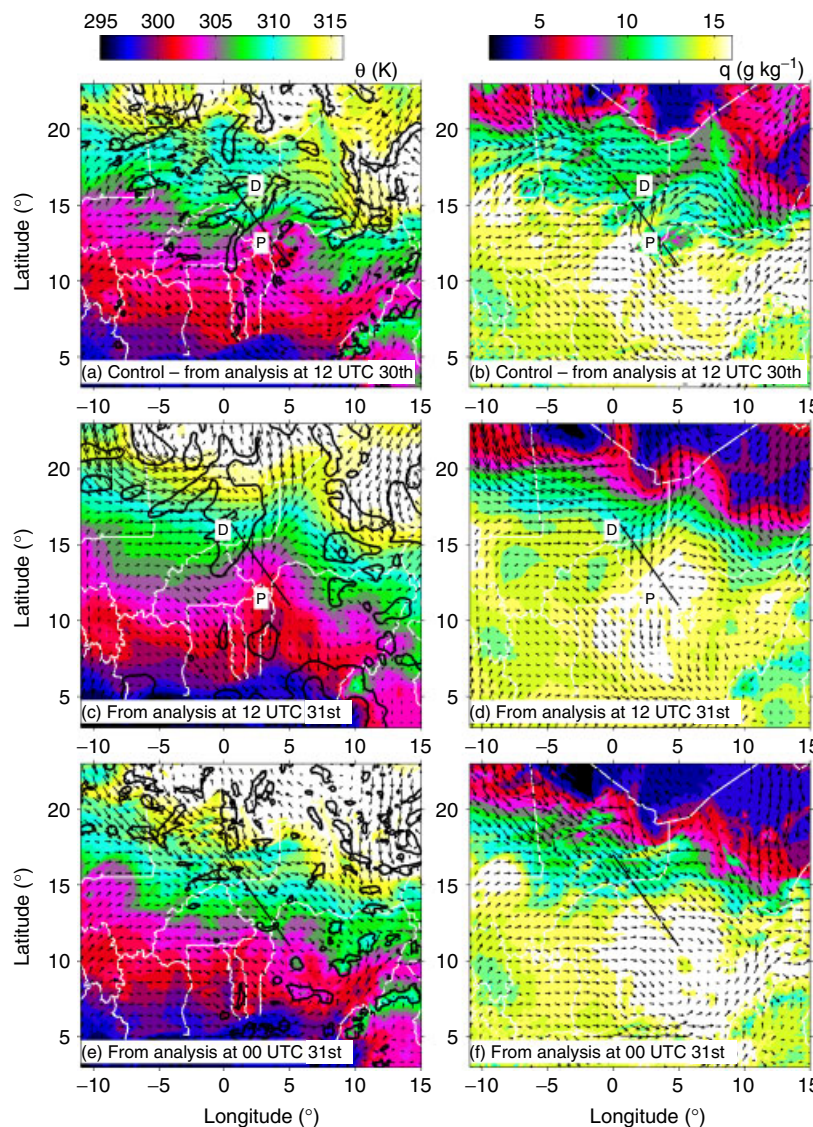


Figure 5. (a), (c) and (e) 925 hPa potential temperature (shading), a contour of 925 hPa convergence (black lines) and 925 hPa wind vectors for the model simulations initialized at 1200 UTC on 30 July (control), 1200 UTC on 31 July and 0000 UTC on 31 July respectively. The contour of convergence in (a) and (e) is at $3 \times 10^{-5} \text{ s}^{-1}$ and in (c) is at $1 \times 10^{-5} \text{ s}^{-1}$. 925 hPa specific humidity (shading) and 925 hPa wind vectors are shown in (b), (d) and (f). All model diagnostics are at 1200 UTC, 31 July 2006. The black diagonal line shows the transect used in other plots. This figure is available in colour online at wileyonlinelibrary.com/journal/qj

diagnostics at 1100 UTC, 31 July (Figure 8). Over the dry soil ($15^\circ\text{N}, 1.7^\circ\text{E}$, solid lines) the boundary layer is deeper (extends to 850 hPa, compared with 925 hPa) and $\sim 6^\circ\text{C}$ warmer than over the wet soil ($16^\circ\text{N}, 1^\circ\text{E}$, dashed lines). Contrary to what would be expected, the lower atmosphere (925 to 650 hPa) is more humid over the dry soil than over the wet soil. This increase in low-level humidity is caused by the monsoon flow, which transports moist air from the south. The monsoon flow does not reach the location of the wet soil ($16^\circ\text{N}, 1^\circ\text{E}$ in Figure 8) and thus the humidity at that location is lower. The higher temperatures (and to a much lesser extent the humidities) over the dry soil cause the CAPE to be approximately double that of the wet soil (1074 J kg^{-1} , compared with 529 J kg^{-1}). CIN is also much lower over the dry soil (16 J kg^{-1} , compared with 163 J kg^{-1}). The low CIN, high CAPE combination of the monsoon air over the dry soil provides suitable conditions for the development of deep convection. It was this thermodynamic profile and the uplift provided by the convergence zone that initiated the convection that later developed into the daughter storm.

Other convective cells initiate later (mainly at 1700 and 1800 UTC, Figure 7), over dry soil, with many developing adjacent to strong gradients in soil moisture. These cells occur due to boundary-layer convergence that develops as a result of the mesoscale circulations, which are caused by the difference in boundary-layer temperatures over the wet and dry soil. These cells initiate later than the daughter storm because they are largely outside the synoptic-scale convergence zone and therefore, the mesoscale circulations require time to develop.

Figure 9 illustrates the change in a number of model diagnostics along a southeast to northwest transect (shown by the straight lines in Figures 5–7) at 1100 UTC. This transect was designed to incorporate both the parent and daughter storm locations, as well as the wet patch at 16°N . The location of the parent storm in both the control and ASSIM simulations is between 11 and 13°N , which is shown by the model medium cloud fraction in Figure 9(a). This storm is precipitating and thus there is wet soil beneath it (Figure 9(b)). The region of wet soil produced by the MCS

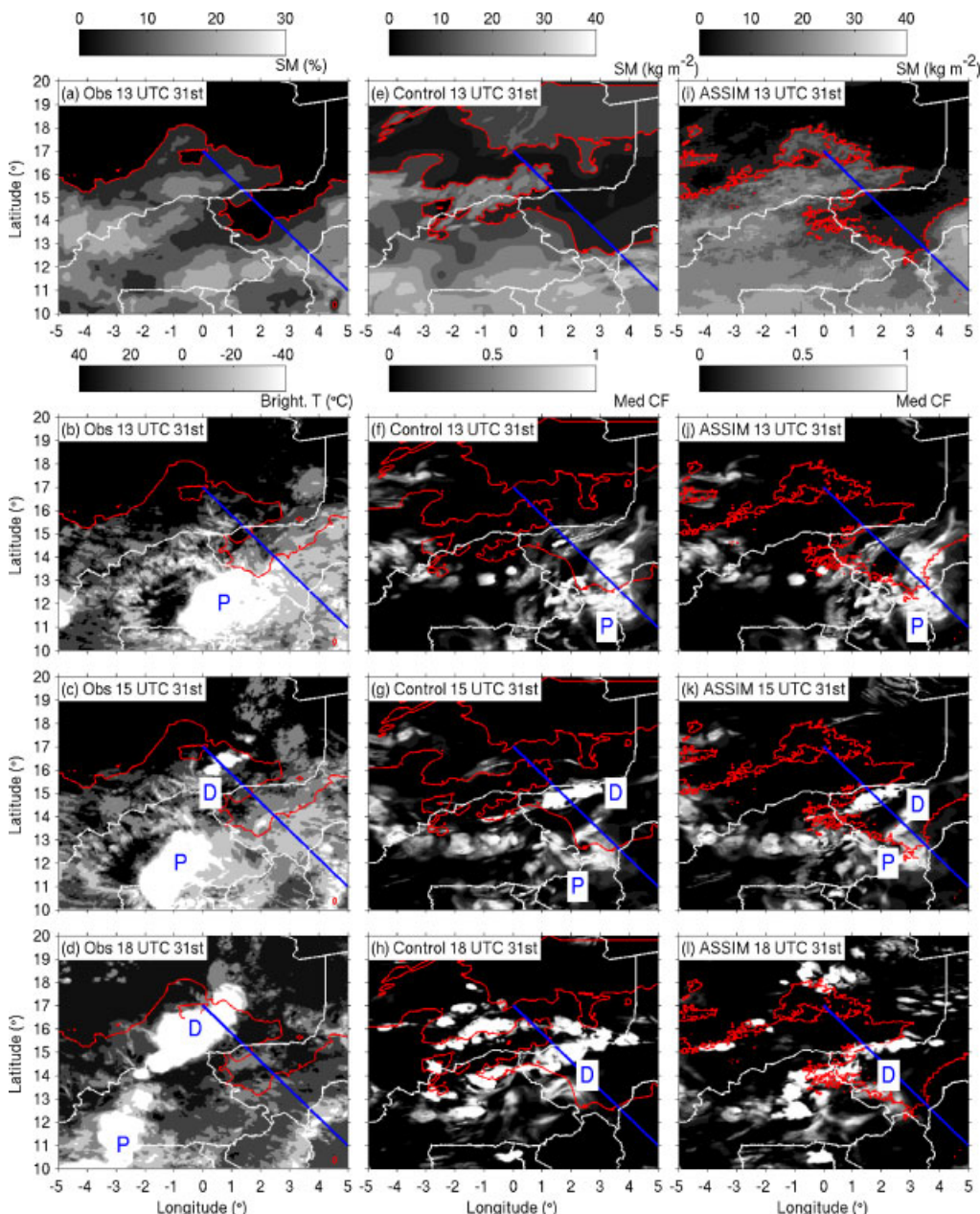


Figure 6. The top panels show soil moisture in the uppermost layer at 1300 UTC, 31 July for (a) the satellite observations, (e) the control simulation and (i) the ASSIM simulation. Note the difference in units between the observed and simulated soil moisture. Panels (b)–(d) show observed soil moisture (contour at 5%) and MSG brightness temperatures. Panels (f)–(h) and (j)–(l) show model soil moisture (contour at 10 kg m^{-2}) and medium cloud fraction (shading). The diagonal line shows the transect used in the other plots. The 'P' and 'D' labels mark the locations of the parent and daughter storms respectively. This figure is available in colour online at wileyonlinelibrary.com/journal/qj

on the previous day is at 16°N . The soil moisture gradients are greater in the control run; the wet patch spans only $\sim 100 \text{ km}$, compared with more than 300 km in the ASSIM experiment. Moisture at the surface has a strong influence on the surface turbulent heat fluxes (Figure 9(c)). In the control run the sensible heat flux (H) is low over the wet soil patch at 16°N and higher over the drier soil to the north. The latent heat flux shows the opposite trend; it is higher over the wet patch at 16°N and lower over the drier soil. The fluxes in the ASSIM simulation are more similar across the soil-moisture gradients; both the sensible and latent heat fluxes vary by less than 150 W m^{-2} over the wet and dry soil.

The differences in soil moisture and surface turbulent heat fluxes induce variations in surface and near-surface temperature. In both simulations the temperatures are higher over the dry soil (Figure 9(d)), although there is

a southeast-to-northwest gradient in temperature between 13.5 and 15.5°N . The variations in specific humidity are less distinct; the soil moisture patches appear to have less of a control on the humidity and the main trend is a southeast-to-northwest decrease, which is due to moisture advection from the south. (Figure 9(e)).

3.3. The cold pool outflow generated by the parent storm

The parent storm generated a cold pool outflow in the model, as observed by Taylor *et al.* (2010). The cold pool can be identified in several of the model diagnostics in Figure 9. The head of the cold pool is associated with a peak in 10 m wind speed, decrease in surface temperature and medium level cloud centred at 13.5°N (Figures 9(f), 9(d) and

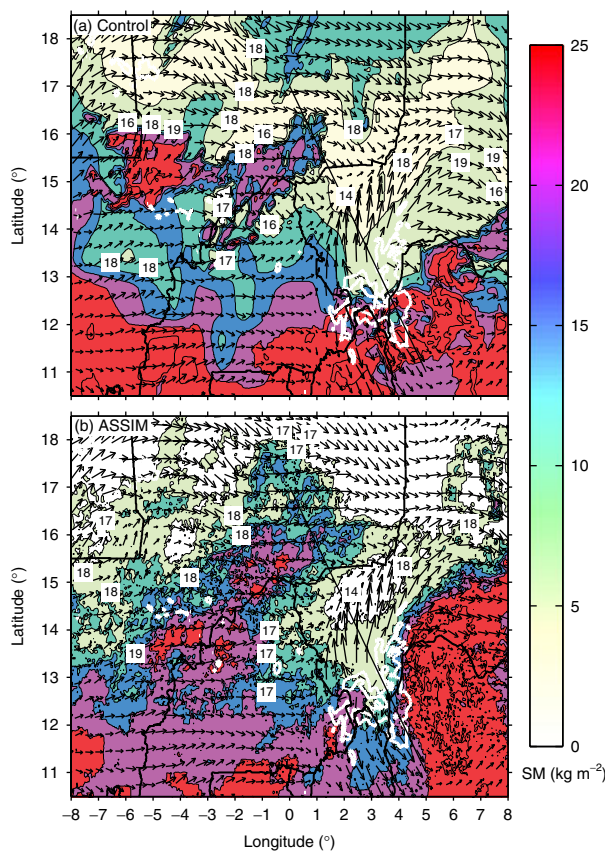


Figure 7. Soil moisture and 925 hPa wind vectors at 1200 UTC, 31 July 2006 from (a) the control run and (b) the ASSIM run at 0600 UTC 31 July 2006. The thick white contour indicates the position of the parent storm at 1200 UTC. The white boxes indicate the locations of the first initiations and contain the times in UTC of the first significant rainfall at each location. The black line shows the diagonal transect. This figure is available in colour online at wileyonlinelibrary.com/journal/qj

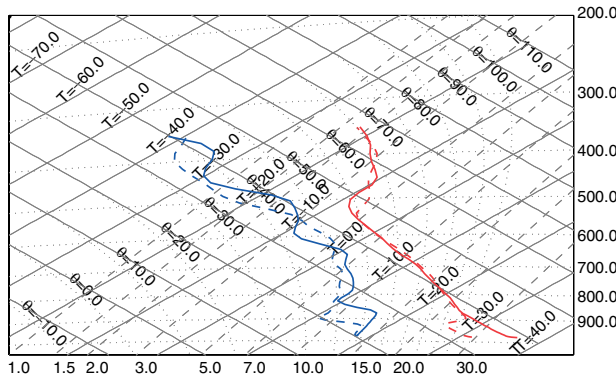


Figure 8. Tephigram of model diagnostics from the control simulation at 1100 UTC, 31 July 2006 over dry soil at 15.0°N, 1.7°E (solid lines) and over the adjacent wet soil at 16.0°N, 1°E (dashed lines). Convective available potential energy values are 1074 J kg⁻¹ over the dry soil and 529 J kg⁻¹ over the wet soil. Convective inhibition values are 16 J kg⁻¹ over the dry soil and 163 J kg⁻¹ over the wet soil. This figure is available in colour online at wileyonlinelibrary.com/journal/qj

9(a) respectively) and with a reduction in specific humidity and an increase in surface fluxes behind this (approximately 0.25° to the south). These perturbations are similar to those observed by Taylor *et al.* (2010, figure 6) and those observed in other tropical oceanic cold pools (e.g. Tompkins, 2001, fig. 18). The passage of the current head decreases the CAPE and increases the CIN of the near-surface air (Figure 9(g)

and (h)), which is largely caused by the changes in near-surface temperature and humidity that are induced by the cold pool.

Figure 10 shows Hovmöller plots of virtual potential temperature, θ_v , and specific humidity, q , at 20 m above ground level, along the southeast to northwest diagonal transect marked in Figures 5–7. The thick white contour shows 100% medium cloud fraction, thus illustrating the location of the parent storm. In the region of dry soil (13–15.5°N) θ_v generally increases through the morning due to increased solar heating. The cold pool decreases the temperature of the near-surface air, it has a lifetime of ~ 3 h and travels approximately 60 km at a speed of $6.9 \pm 0.5 \text{ m s}^{-1}$ towards the northwest (white dashed line). By 1300 UTC the large turbulent heat fluxes at the surface have greatly reduced its strength and north of 14.25°N any buoyancy decrease from the cold pool is undetectable. It is possible that the cold pool does not progress far past the edge of the wet soil at 13.5°N because the large sensible heat flux over the dry soil leads to a rapid mixing away of the density gradient.

The specific humidity Hovmöller plot (Figure 10(b)) shows that at 0600 UTC the boundary-layer air over the dry soil (13.5–15°N) is more humid than over the wetter soil to the north. This is due to the strong southerly monsoon flow shown in Figure 5(a). The high humidity persists through to the afternoon, except for the southeastern edge, where the humid air is replaced by drier air in the cold pool.

3.4. The role of waves generated by the parent storm in triggering convection

The influence of the atmospheric waves emitted by the parent storm was found to be very similar in the control and ASSIM simulations. For this reason the remainder of the section uses diagnostics from only the control run to investigate the role of waves in the triggering of the daughter storm. Figure 11 shows plots of vertical velocity in the initiation region of the daughter storm at 0900 and 1100 UTC, 31 July 2006. The location of the parent storm ('P') is indicated by the region of significant up- and downdrafts south of 13°N. The daughter storm initiation location is to the north of this and is marked on the plot by the black 'X'. Two significant waves are emitted from the parent storm in the early hours of the morning. The first wave (W1, indicated by the line of positive vertical velocity and the black dashed line) is emitted at approximately 0600 UTC and propagates away from the parent storm, towards the northwest. By 0900 UTC it is approximately 100 km away from the daughter storm initiation location (Figure 11(a)). The second wave (W2) is emitted from the parent storm at approximately 0900 UTC and also propagates towards the northwest. By 1100 UTC, W1 has reached the daughter storm initiation location and W2 is approximately 100 km to the southeast (Figure 11(b)).

The structure, propagation and effect of the waves are illustrated using plots of θ_v , vertical velocity and medium cloud fraction along the diagonal transect (Figures 12 and 13). At 0800 UTC, 31 July 2006 the parent storm is between 12 and 13.5°N, which is shown by the high levels of medium cloud in Figure 12(a) and the region of intense up- and downdrafts in Figure 12(b). The wet soil associated with the parent storm is illustrated by the dashed line in Figure 12(a) and the wet patch to the northwest is also shown between 15.7 and 16.4°N.

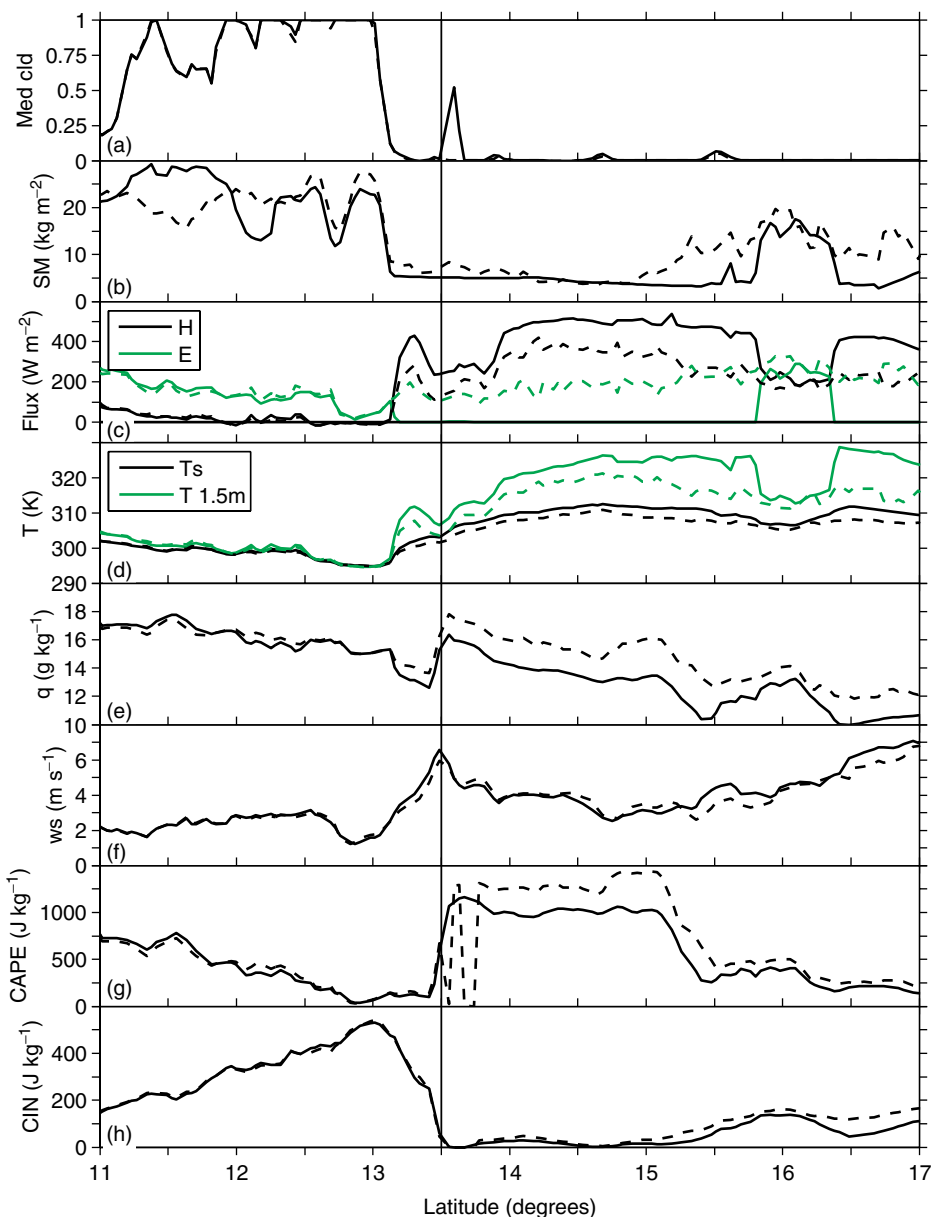


Figure 9. Variables at 1100 UTC, 31 July 2006 along the diagonal: (a) medium cloud fraction, (b) soil moisture in the uppermost layer, (c) surface sensible (H) and latent (E) heat fluxes, (d) surface (T_s) and near-surface ($T_{1.5m}$) temperatures, (e) near-surface specific humidity, (f) 10 m wind speed, (g) convective available potential energy (CAPE), (h) convective inhibition (CIN). Solid lines represent diagnostics from the control and the dashed lines represent diagnostics from the ASSIM simulation. The vertical black line marks the position of the cold pool on the diagonal section. This figure is available in colour online at wileyonlinelibrary.com/journal/qj

Away from the parent storm the boundary layer is 0.8 to 1 km deep at 0800 UTC (Figure 12(b)). The peak in boundary-layer temperatures at the daughter storm initiation location ($\sim 14.9^\circ\text{N}$) and the minimum in boundary-layer temperatures over the wet soil patch ($\sim 16^\circ\text{N}$) are already evident. The first wave, W1, is emitted from the parent storm at approximately 0600 UTC and propagates towards the northwest (left to right in the transect plots) between 0800 and 1000 UTC (Figures 12(b)–12(d)). The first wave, W1, extends from the top of the CBL up to at least 8 km and is most prominent in the parts of the atmosphere with higher stability, that is, 1–3 km and above 5.5 km, on either side of the near-neutrally stratified SAL. As it propagates towards the northwest W1 does not produce cloud (solid lines, Figure 12(a)).

By 1100 UTC a cooler, shallower boundary layer is evident over the wet patch between 15.5 and 16.5°N and the shallow

convection associated with the daughter storm is readily seen at 14.9°N (Figure 13(b)). The extent of the cold pool associated with the parent storm is also shown in Figures 12(d) and 13(b)–(d). It does not propagate further north of 13.9°N . The first wave, W1, reaches the region of shallow convection at approximately 1100 UTC (14.8°N , Figure 13(b)). Cloud begins to form over this region between 1100 and 1200 UTC (black and red solid lines respectively, Figure 13(a)) but deep convection does not initiate at this time. The second wave, W2, is emitted from the parent storm at approximately 0900 UTC and is visible in Figure 13(b) at 14°N . This second wave also propagates towards the northwest and reaches the region of shallow convection at 14.8°N at 1300 UTC. At this point deep convection is initiated and a large amount of cloud begins to form.

The structure of W1 and W2 is reasonably similar. Both waves cause upward displacement of air in the lower

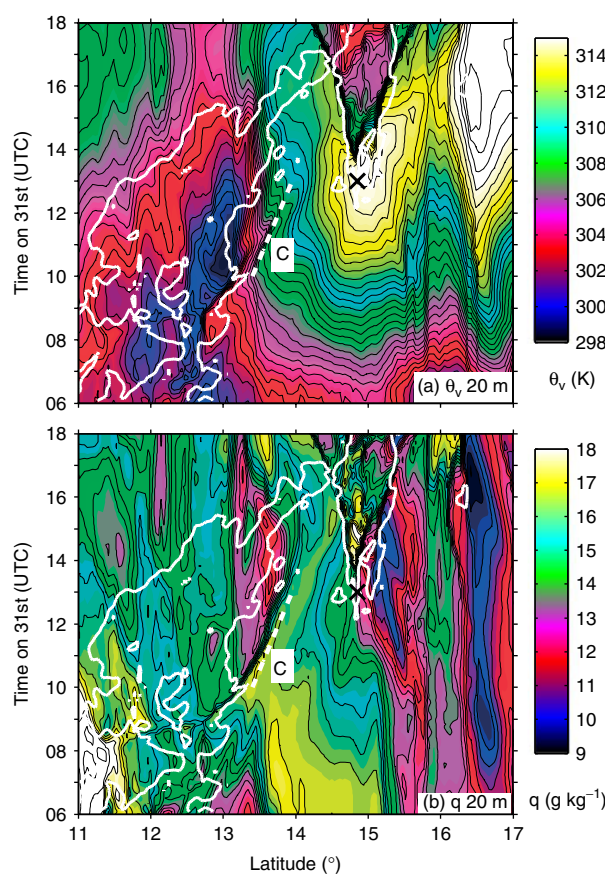


Figure 10. Hovmöller plot of (a) θ_v and (b) specific humidity at 20 m above ground level along the diagonal transect. The thick white contour shows 100% medium cloud fraction. The dashed white line indicates the propagation of the cold pool (C). The time and location of the initiation of deep convection in the daughter storm is marked by the black cross. This figure is available in colour online at wileyonlinelibrary.com/journal/qj

atmosphere (below 4 km for W1 and below 5.5 km for W2) and downward displacement of air in the upper troposphere. This has the potential to lift air parcels above their level of free convection and initiate deep convection.

Hovmöller plots of θ_v and medium cloud fraction, along the diagonal transect marked in Figures 5–7, at 2 and 6 km above mean sea level can be used to illustrate the propagation of the waves and their effect on the initiation of deep convection (Figure 14). The dashed white lines (labelled W1 and W2) indicate the propagation of the two waves, diagnosed from the Hovmöller plots themselves and an animation of cross-section plots at 5 min intervals, similar to those in Figures 12 and 13. The parent storm is illustrated by the solid white contours between 11 and 13°N and the initiation of the daughter storm is shown by the white contours and black crosses at 14.9°N. The first wave travels at $15.7 \pm 0.5 \text{ m s}^{-1}$ (compared with Taylor *et al.* (2010)'s observed speed of $\sim 13 \text{ m s}^{-1}$) and reaches the region of shallow convection at 1100 UTC. The propagation of W1 causes upward displacement of air in the lower atmosphere ($< 4 \text{ km}$); this is illustrated by the θ_v cross-sections in Figure 12 and by the lower values of θ_v behind the wave in Figure 14(a).

Figure 15(a) shows a Hovmöller plot of CIN along the diagonal transect. Northwest of the parent storm ($> 13^\circ\text{N}$) CIN is reduced during the morning due to increased mixing caused by diurnal heating. The first wave also decreases

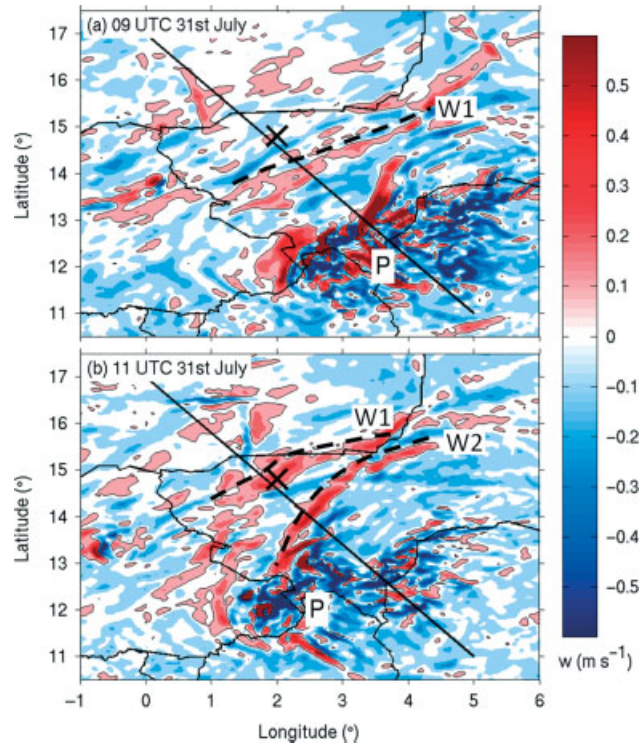


Figure 11. 700 hPa vertical velocity at (a) 0900 UTC and (b) 1100 UTC, 31 July 2006. The single black contour is at 0.1 m s^{-1} . The black dashed lines indicate the leading edge of the two waves (W1 and W2). The 'P' indicates the location of the parent storm, the black cross the daughter storm initiation point and the black line the diagonal transect.

CIN, although the changes are only significant between 13 and 14.5°N . By the time W1 reaches the daughter storm initiation point (14.8°N) CIN is already very close to zero. Very low CIN is, however, not the only prerequisite for the initiation of deep convection; a source of uplift is required. The first wave does provide uplift but it does not provide enough to initiate deep convection. It does, however, bring air to its lifting condensation level (LCL) and cloud begins to form (Figure 13(a), red line). The influence of W1 on the LCL is illustrated in Figure 15(b), which shows the actual pressure, p , at 3000 m above MSL, minus the pressure at which the air at 3000 m would have to be lifted to in order to reach its LCL, p_{LCL} , that is, when $p - p_{\text{LCL}}$ is large the air at 3000 m is much lower (in altitude) than its LCL. As $p - p_{\text{LCL}}$ decreases, the air at 3000 m becomes closer to its LCL, until $p - p_{\text{LCL}} = 0$, at which point water in the air is able to condense and form clouds. This plot shows that W1 brings air at 3000 m to its LCL, that is, provides enough uplift to allow shallow convection to commence.

The second wave propagates northwestwards at the faster speed of $19.3 \pm 0.5 \text{ m s}^{-1}$. Like W1, this wave also causes upward displacement of air in the lower atmosphere (Figure 14(a)). It reaches the region of shallow convection at 1300 UTC, coinciding exactly with the development of deep convection (shown by the black crosses on Figure 14 and the development of a significant amount of medium cloud at 14.9°N). Compared with the first wave, the second wave arrives at a time when the mixing in the boundary layer is deeper and where shallow, moist convection already exists. Therefore, W2 is able to provide enough uplift to trigger deep convection.

An additional instance of wave-generated secondary initiation at 16.3°N at 1600 UTC is illustrated in Figure 14(b).

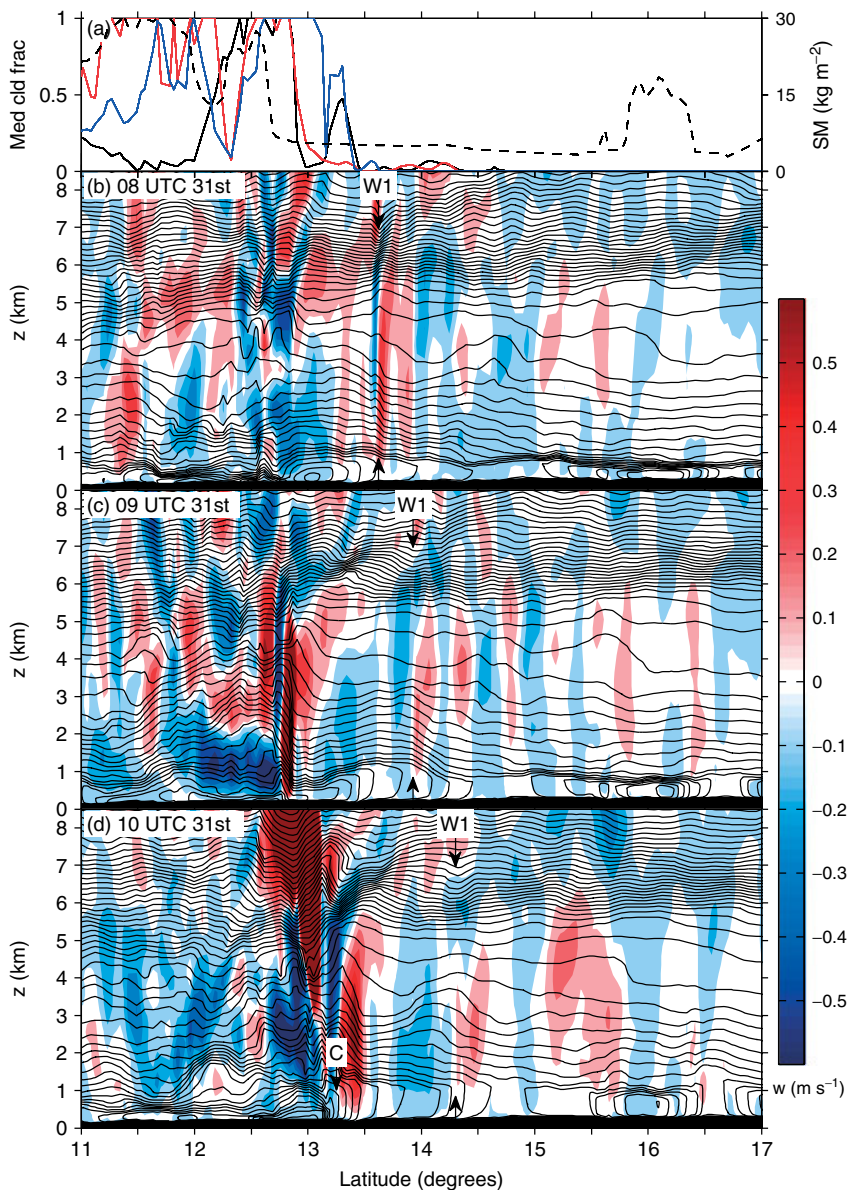


Figure 12. (a) Soil moisture (dashed line) and medium cloud fraction at 0800 UTC (black line), 0900 UTC (red line) and 1000 UTC (blue line). (b)–(d) Vertical velocity (shading) and virtual potential temperature (black contours at 0.75 K intervals). All diagnostics are from the control simulations and are along the diagonal transect. The arrows mark the position of the first wave (W1) and the cold pool (C).

A wave is emitted from the daughter storm between 1400 and 1500 UTC and propagates towards the region of shallow convection at 16.5°N (W3), which is over dry soil on the far side of the wet patch (shown in Figure 13). When W3 reaches the shallow convection at 1600 UTC, the appearance of cloud in Figure 14(b) shows that deep convection is triggered. This wave is not evident in the θ_v field at 2 km because the waves only propagate in stratified regions of the atmosphere and by mid-afternoon the CBL extends to above 2 km.

3.5. The character of the convectively generated waves

The schematic in Figure 16 summarizes the propagation of the observed and simulated waves and cold pools. Deep convection in the observed daughter storm initiated in the region around 16.5°N, 1°E at 1300 UTC. Taylor *et al.* (2010) suggest that this coincided with the arrival of a gravity wave that was emitted from the parent storm to the southeast

(Figure 16, green lines). The only evidence for this wave was a band of high, cold cloud that was observed in the satellite imagery, which propagated northwestwards from the parent storm. There was also a cold pool associated with the observed parent storm, which also propagated towards the northwest, but at a slower rate compared with the wave (light grey dashed lines).

In the model simulation, deep convection associated with the daughter storm developed at 1300 UTC in the region 14.5°N, 2°E. Like the observations, this coincided with the arrival of a gravity wave (W2) from the simulated parent storm (Figure 16, blue lines). A cold pool was also simulated by the model, which like the observations, propagated towards the northwest but did not directly affect the initiation of deep convection in the daughter storm (dark grey dashed lines).

There are two main differences between the observed wave features and those simulated by the model. First, the earlier wave in the model (W1, red lines) is not evident

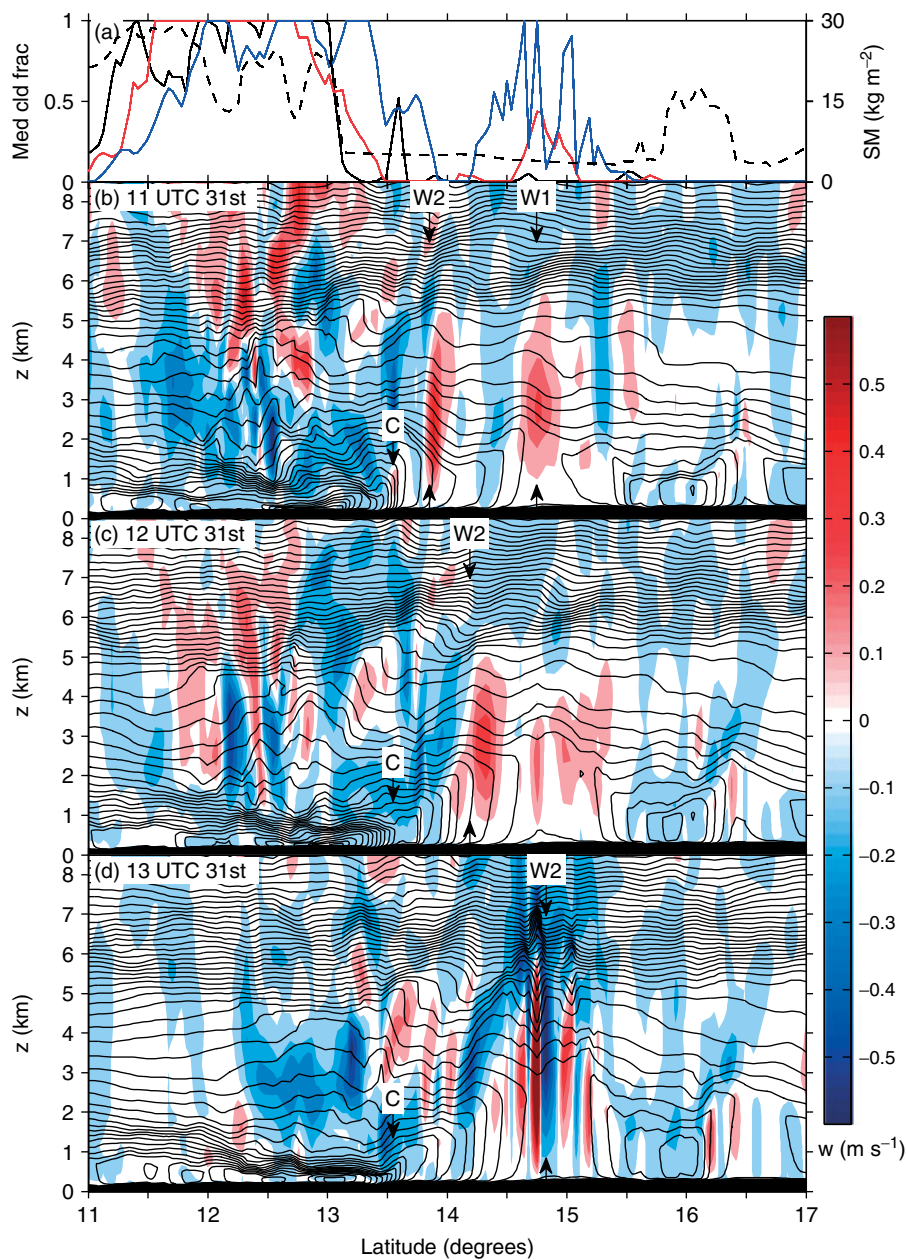


Figure 13. Same as Figure 12 but for 1100, 1200 and 1300 UTC. The black, red and blue lines in (a) represent the medium cloud fraction at 1100, 1200 and 1300 UTC respectively.

in the observations. Either it did not occur in reality, or it did not produce sufficient cloud to be visible in the satellite imagery. Second, the location of the daughter storm and associated waves all occur approximately 100 km to the southeast of where they occurred in reality. The parent MCS in the model simulation was also approximately 100 km further south than the observed parent MCS at the time the waves were emitted (not shown). Although the location of the entire model parent–daughter system was displaced by some distance compared with the observations, the speed of the model waves, the distance between the parent and daughter storm and the arrival time of W2 at the daughter storm initiation location was in very good agreement with the observations.

Taylor *et al.* (2010) speculate about the type of wave that propagated outwards from the parent storm. The wave could have been either: (i) a nonlinear ‘bore’ or solitary type wave, that was caused by the cold pool and propagated along

the CBL and SAL interface; or (ii) a wave-front that was not confined to the lower atmosphere. The θ_v and vertical velocity sections (Figures 12 and 13) and the Hovmöller plot in Figure 14(b) show that neither of the model waves were confined to low levels. They both produced upward displacement of air in the lower atmosphere (< 5 km) and downward displacement of air in the free troposphere (> 5.5 km). The waves in the model appear to take the form of a wave-front, rather than a bore that resides on the CBL–SAL interface. The model wave does not produce any cloud as it propagates northwestwards until it reaches the region of shallow convection associated with the parent storm. It is possible that either: (i) the model reproduces the wave structure as it occurred in reality but it does not produce the associated cloud; or (b) the wave structure in the model does not represent the exact observed structure.

The W1 and W2 waves in the simulation performed for this study travel at similar speeds and appear to take the

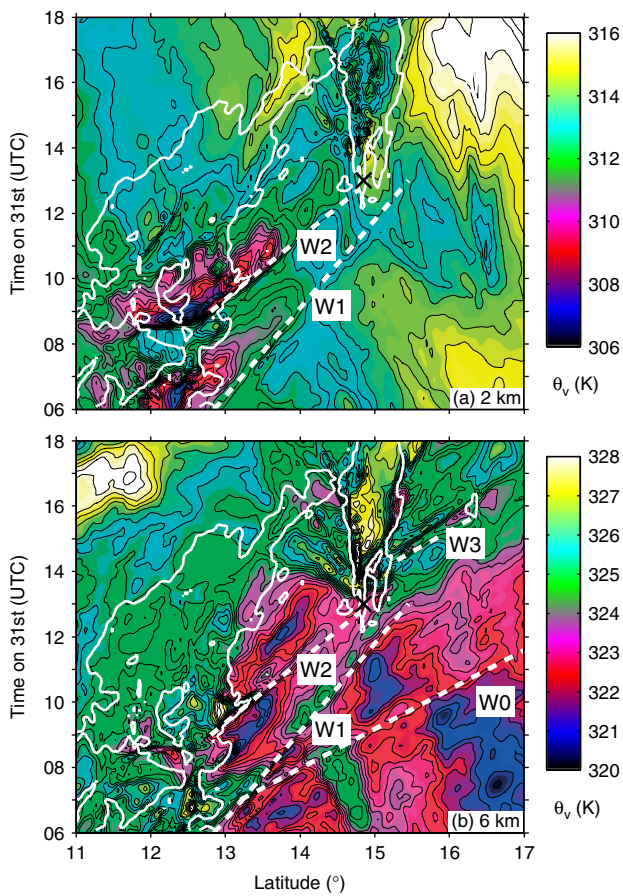


Figure 14. Hovmöller plots of θ_v along the diagonal transect at (a) 2 km and (b) 6 km above mean sea level. The white contour shows 100% medium cloud fraction. The white dashed lines indicate the waves (W₀–W₃). The time of the initiation of deep convection in the daughter storm is marked by the black cross. This figure is available in colour online at wileyonlinelibrary.com/journal/qj

form of an $n = 2$ mode wave. Like the $n = 2$ mode in Lac *et al.* (2002), but opposite to the $n = 2$ waves in Lane and Reeder (2001) and Marsham and Parker (2006), W1 and W2 cause upward displacement in the lower atmosphere and downward displacement in the upper atmosphere. The vertical wavelength (λ_z) of a wave can be estimated using the equation:

$$\lambda_z = \frac{n\pi c}{N} \quad (1)$$

where n is the wave mode, c is the phase speed and N is the Brünt–Väisälä frequency. Assuming $n = 2$, $c = 17.5 \text{ m s}^{-1}$ (mean of the W1 and W2 speeds) and a mean value of N over the troposphere of $\sim 0.01 \text{ s}^{-1}$, gives a vertical wavelength of $\sim 11 \text{ km}$, which is approximately equal to the depth of the troposphere in this case.

A third wave is indicated on the θ_v Hovmöller plot at 6 km in Figure 14(b) (W0). It is emitted from the parent storm at approximately the same time as W1, but it travels faster ($33.5 \pm 0.5 \text{ m s}^{-1}$, compared with $15.7 \pm 0.5 \text{ m s}^{-1}$ for W1 and $19.3 \pm 0.5 \text{ m s}^{-1}$ for W2). The maximum displacement occurs aloft and is therefore visible only in the 6 km Hovmöller plot. This wave may be the $n = 1$ mode because it is approximately twice as fast (33.5 m s^{-1}) as the W1 and W2 waves.

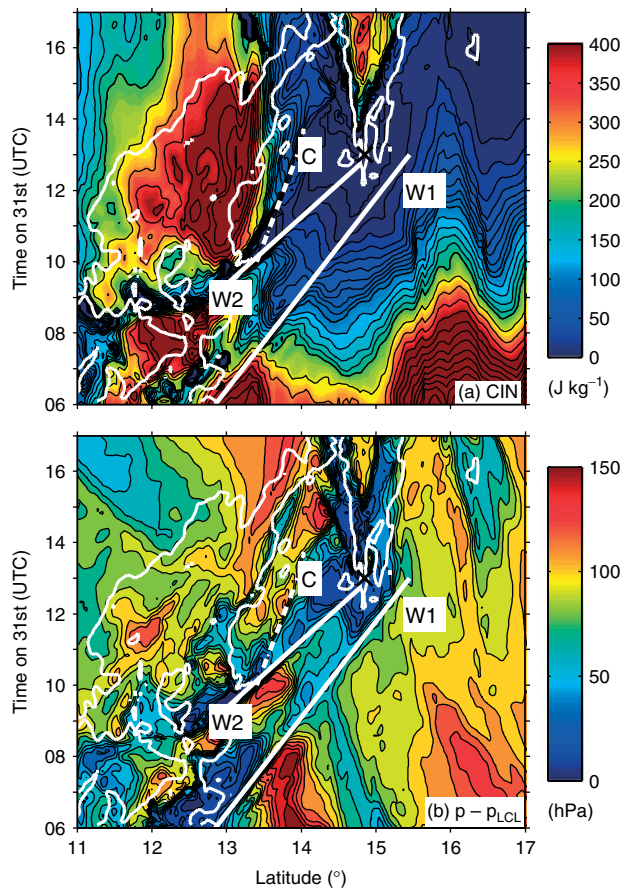


Figure 15. Hovmöller plots along the diagonal transect of (a) convective inhibition (CIN), where contours are at 50 J kg^{-1} intervals above 200 J kg^{-1} , at 20 J kg^{-1} intervals above 100 J kg^{-1} and at 10 J kg^{-1} below 100 J kg^{-1} and (b) the pressure at 3000 m minus the pressure of the lifting condensation level, where contours are at 10 hPa intervals. The thick white contour shows 100% medium cloud fraction. The dashed white line indicates the propagation of the cold pool (C) and the white lines indicate the two waves (W1 and W2). The time of the initiation of deep convection in the daughter storm is marked by the black cross.

4. The relative importance of the different triggering mechanisms

The model control simulation shows that the land surface and gravity waves are influential in the development of new convection. One of the additional simulations described in section 3.1, which was initialized at 1200 UTC 31 July (24 h later than the control), is a good test of the importance of these trigger mechanisms because it does not reproduce the soil-moisture heterogeneity or the gravity waves associated with the parent storm.

Figure 17(a) shows the model soil-moisture diagnostic at 1300 UTC, 1 h after the initialization. The large-scale north–south soil moisture gradient is similar to that in the control, but the wet patch that was created by the MCS on 30 July is missing (compare with Figure 6(e)). Figures 17(b)–17(d) show the development of the parent and daughter storms in this simulation. The parent storm is in the south of the domain and the daughter storm develops over the dry soil, in a location approximately 150 km to the northwest of the daughter storm in the control and in a position that is closer to that observed (compare Figure 17(c) with Figures 6(c) and (g)). The location is more accurate because the analysis gives a better representation of the synoptic-scale convergence zone. A

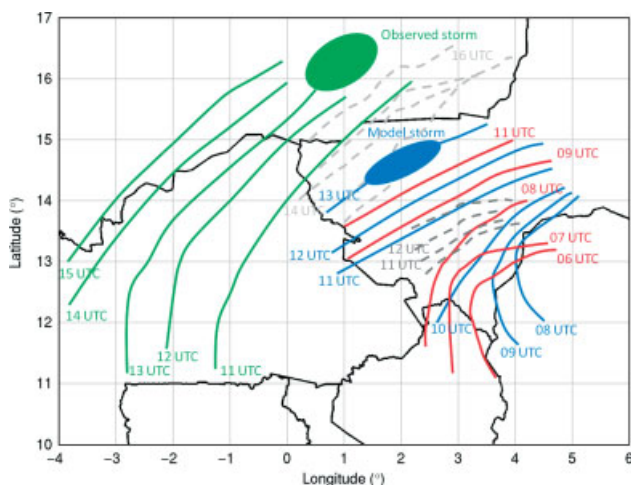


Figure 16. Schematic of the gravity waves and cold pools associated with this case study. The observed gravity wave is shown by the solid green lines and the observed cold pool by the light grey dashed lines. The first and second model gravity waves are shown by the solid red and blue lines respectively and the dark grey dashed lines show the model cold pool.

sensitivity test was performed on the control, where the soil moisture was smoothed to its mean value over the region where the daughter storm initiated (not shown). In this case the daughter storm did not develop because the surface was not hot enough to produce deep mixing. It seems that the soil moisture patterns determine the exact structure of the developing storm but as long as there is some dry soil present, the synoptic-scale dynamics are a more important trigger mechanism.

The daughter storm in Figure 17 develops approximately 5 h later in the day than in the control run and the observations. Although the parent storm is present in the simulation, no significant gravity waves are emitted from it (not shown). Time is required for convective-scale circulations to ‘spin-up’ in the 4 km simulations, but this 5 h delay in the formation of deep convection highlights the important role of the convectively generated waves that triggered the storm in the control run. The analysis in section 3.4 shows that the arrival of a gravity wave coincides exactly with the initiation of deep convection. These waves may not be the determining factor in whether a storm is initiated or not, but they do influence the timing of the initiation of deep convection and therefore the timing of the development of a storm into a MCS.

These findings are in agreement with Guichard *et al.* (2010), who show that the initial and boundary conditions significantly control the locations of rainfall over West Africa, and that explicit moist convection improves the precipitation distribution, MCS trajectory and propagation speed but cannot correct for weaknesses in the analysis. Klüpfel *et al.* (2011b) also suggest that the boundary-layer convergence zone was the most important triggering mechanism for this case. It seems that as long as there is some dry soil present, the synoptic-scale dynamics is the most important trigger mechanism, with the gravity wave from the parent storm and the soil moisture patterns being of secondary influence. If the model captures the large-scale environment accurately, the soil-moisture heterogeneity determines the exact location of the initiation of the storm and the gravity waves determine the timing of the development of deep convection.

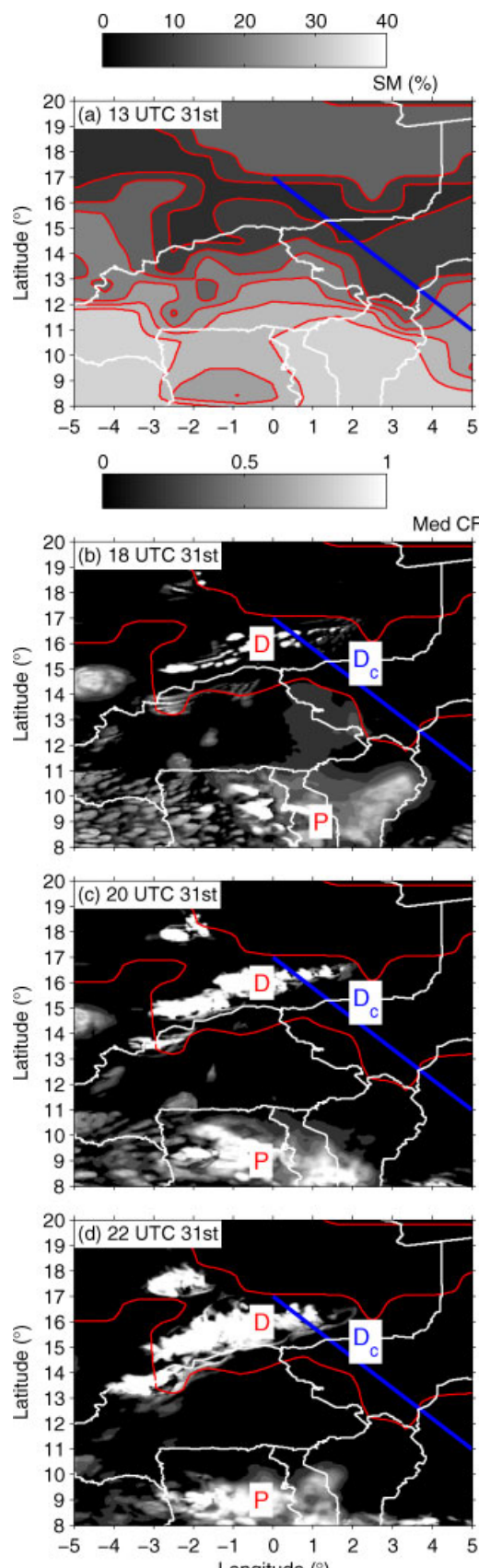


Figure 17. (a) Soil moisture at 1300 UTC, (b)–(d) medium cloud fraction at 18, 20 and 2200 UTC and a contour of soil moisture at 10 kg m^{-2} for the model run initialized at 1200 UTC, 31 July 2006. The diagonal line marks the transect used in the analysis of the control; ‘Dc’ marks the location of the initiation of the daughter storm in the control; ‘D’ and ‘P’ mark the locations of the daughter and parent storms in this run. This figure is available in colour online at wileyonlinelibrary.com/journal/qj

5. Summary

This study shows that the MetUM, run with explicit convection at 4 km horizontal resolution, is able to reproduce the key aspects of a mesoscale convective system (MCS) observed in the Sahel during summer (Taylor *et al.*, 2010). The 4 km model simulations were very sensitive to the analyses used in the initialization; two of the runs produced the case study well and one was unsuccessful. This appears to be due to differences in the way the analyses represent convergence zones caused by the confluence of cyclonic circulations around the Saharan heat low with the moist, southerly monsoon flow.

Similar to the observations, a MCS develops in the control simulation on 30 July and creates the wet soil patches in the case-study storm initiation region, before dissipating during the early hours of 31 July. A second MCS (the ‘parent’ storm) also develops on 30 July, although this persists through the night until the afternoon of 31 July. In the model the main ‘daughter’ storm develops at ~1300 UTC on 31 July, over dry soil, in a synoptic-scale convergence zone, enhanced by the circulation created by the parent MCS. Although this initiation appears less related to soil-moisture boundaries than in the observations of Taylor *et al.* (2010), other convective cells develop later in the afternoon (1700 and 1800 UTC) on dry soil, but adjacent to strong soil-moisture gradients: the locations of these cells are consistent with boundary-layer convergence associated with mesoscale circulations caused by soil-moisture variations. During the evening the daughter storm and the other convective cells merge to form the case study MCS, whereas the observations show that the case study MCS initiated at one point and then grew in size.

Taylor *et al.* (2010) suggest that a gravity wave that is emitted from the parent storm played a part in the development of deep convection in the daughter. In the model simulations two pronounced waves are emitted from the parent storm between 0600 and 0900 UTC on 31 July. The first wave is emitted from the parent storm at approximately 0600 UTC, it propagates towards the northwest and reaches the region of shallow convection associated with the daughter storm at 1100 UTC. This wave generates shallow cloud at the initiation location of the daughter storm but does not initiate deep convection. The second wave is emitted from the parent storm at approximately 0900 UTC and reaches the daughter storm at 1300 UTC. Boundary-layer mixing is more intense by this time and the arrival of the wave coincides exactly with the development of deep convection in the daughter storm.

Both these waves appear to be wave-fronts that propagate throughout the depth of the free troposphere, rather than a bore-like wave which Taylor *et al.* (2010) suggest may have propagated along the stable interface between the convective boundary layer and near-neutral SAL aloft. The model waves cause upward displacement of air in the lower half of the troposphere and downward displacement of air in the upper troposphere. This suggests that the waves are of $n = 2$ mode, with a vertical wavelength equal to the depth of the troposphere. This interpretation is supported by weaker evidence of a deep $n = 1$ mode in the model, which travels approximately twice as fast as the $n = 2$ waves that trigger the convection.

This study suggests that there are three aspects that need to be represented accurately in a model in order to be able to

predict this kind of system. First, the large-scale circulation and thermodynamic profile must be representative, which requires a good quality atmospheric analysis to initialize the forecast. Second, if the location of the initiation of the system is to be forecast accurately, the spatial variability of land surface properties (notably soil moisture) must be accurate. Finally, in order to reproduce the timing of secondary initiation correctly the model must be able to capture gravity waves that are emitted by existing systems.

Acknowledgement

The authors would like to thank Caroline Bain, Sean Milton and Bethan White for fruitful discussions and suggestions and two anonymous reviewers for their helpful comments and suggestions. We are grateful to the National Centre for Atmospheric Science (NCAS) Computer Modelling Service for help with model configurations, initialization data and general enquires. We would like to thank EUMETSAT for the cloud data, Le Laboratoire de Météorologie Dynamique for the EPSAT-SG precipitation data and Thierry Pellarin for the AMSR-E/EPSAT-SG surface soil moisture product. We also acknowledge the TRMM mission scientists and associated NASA personnel for the production of the TRMM data used in this article and are grateful to the Goddard Earth Sciences Data and Information Services Center (GES DISC) for making the data available. The work has been supported by NERC Grants NE/B505538/1, NE/G018499/1 and NE/E003826/1. Based on a French initiative, AMMA was built by an international scientific group and is currently funded by a large number of agencies, especially from France, United Kingdom, USA and Africa. It has been the beneficiary of a major financial contribution from the European Community’s Sixth Framework Research Programme. Detailed information on scientific coordination and funding is available on the AMMA International web site <http://www.ammainternational.org>.

References

- Adler B, Kalthoff N, Gantner L. 2011. The impact of soil moisture inhomogeneities on the modification of a mesoscale convective system: An idealised model study. *Atmos. Res.* **101**: 354–372.
- Agustí-Panareda A, Balsamo G, Beljaars A. 2010a. Impact of improved soil moisture on the ECMWF precipitation forecast in West Africa. *Geophys. Res. Lett.* **37**: L20808, DOI:10.1029/2010GL044748.
- Agustí-Panareda A, Beljaars A, Ahlgrimm M, Balsamo G, O B, Forbes R, Ghelli A, Guichard F, Köhler Meynadier R, Morcrette JJ. 2010b. The ECMWF re-analysis for the AMMA observational campaign. *Q. J. R. Meteorol. Soc.* **136**: 1457–1472.
- Agustí-Panareda A, Beljaars A, Cardinali C, Genkova I. 2010c. Impacts of assimilating AMMA soundings on ECMWF analyses and forecasts. *Wea. Forecast.* **25**: 1142–1160.
- Anabor V, Stensrud DJ, de Moraes OLL. 2009. Simulation of a serial upstream-propagating mesoscale convective system event over southeastern South America using composite initial conditions. *Mon. Weath. Rev.* **137**: 2144–2163.
- Bergés JC, Jobard L, Chopin F, Roca R. 2010. EPSAT-SG: a satellite method for precipitation estimation; its concepts and implementation for the AMMA experiment. *Ann. Geophys.* **28**: 289–308.
- Beres JH, Alexander MJ, Holton JR. 2002. Effects of tropospheric wind shear on the spectrum of convectively generated gravity waves. *J. Atmos. Sci.* **59**: 1805–1824.
- Best MJ, Pryor M, Clark DB, Rooney GG, Essery RLH, Ménard CB, Edwards JM, Hendry MA, Porson A, Gedney N, Mercado LM, Sitch S, Blyth E, Boucher O, Cox PM, Grimmond CSB, Harding RJ. 2011. The Joint UK Land Environment Simulator (JULES), model description – Part 1: Energy and water fluxes. *Geosci. Model Dev.* **4**: 677–699.

- Boone A, de Rosnay P, Balsamo G, Beljaars A, Chopin F, Decharme B, Delire C, Ducharne A, Gascoin S, Grippa M, Guichard F, Gusev Y, Harris P, Jarlan L, Kergoat L, Mougin E, Nasonova O, Norgaard A, Orgeval T, Ottlé C, Poccard-Leclercq Polcher J, Sandholt I, Saux-Picart S, Taylor C, Xue Y. 2009. The AMMA land surface model intercomparison project (ALMIP). *Bull. Am. Meteorol. Soc.* **90**: 1865–1880.
- Bretherton CS, Smolarkiewicz PK. 1989. Gravity waves, compensating subsidence and detrainment around cumulus clouds. *J. Atmos. Sci.* **46**: 740–759.
- Carleton AM, Adegoke J, Allard J, Arnold DL, Travis DJ. 2001. Summer season land cover – convective cloud associations for the Midwest US ‘Corn Belt’. *Geophys. Res. Lett.* **28**: 1679–1682.
- Charba J. 1974. Application of gravity current model analysis of squall-line gust front. *Mon. Weath. Rev.* **102**: 140–156.
- Crook NA, Miller MJ. 1985. A numerical and analytical study of atmospheric undular bores. *Q. J. R. Meteorol. Soc.* **111**: 225–242.
- Davies T, Cullen MJP, Malcolm AJ, Mawson MH, Staniforth A, White AA, Wood S. 2005. A new dynamical core for the Met Office’s global and regional modelling of the atmosphere. *Q. J. R. Meteorol. Soc.* **131**: 1759–1782.
- Droegemeier KK, Wilhelmsson RB. 1985a. Three-dimensional numerical modeling of convection produced by interacting thunderstorm outflows. Part I: Control simulation and low-level moisture variations. *J. Atmos. Sci.* **42**: 2381–2403.
- Droegemeier KK, Wilhelmsson RB. 1985b. Three-dimensional numerical modeling of convection produced by interacting thunderstorm outflows. Part II: Variations in vertical winds shear. *J. Atmos. Sci.* **42**: 2404–2414.
- Emanuel KA. 1994. *Atmospheric Convection*. Oxford University Press.
- Emori S. 1998. The interaction of cumulus convection with soil moisture distribution: An idealized simulation. *J. Geophys. Res.* **103**: 8873–8884.
- Essery RLH, Best MJ, Cox PM. 2001. MOSES 2.2 Technical Documentation. Technical Report, Met Office: Exeter; 14 August.
- Gaertner MA, Domiguez M, Garvert M. 2010. A modelling case-study of soil moisture–atmosphere coupling. *Q. J. R. Meteorol. Soc.* **136**: 483–495.
- Gantner L, Kalthoff N. 2010. Sensitivity of a modelled life cycle of a mesoscale convective system to soil conditions over West Africa. *Q. J. R. Meteorol. Soc.* **136**: 471–482.
- Garcia-Carreras L, Parker DJ, Marsham JH. 2011. What is the mechanism for the modification of convective cloud distributions by land surface-induced flows? *J. Atmos. Sci.* **68**: 619–634.
- Goff RC. 1976. Vertical structure of thunderstorm outflows. *Mon. Weath. Rev.* **104**: 1429–1440.
- Goler RA, Reeder MJ. 2004. The generation of the Morning Glory. *J. Atmos. Sci.* **61**: 1360–1376.
- Gregory D, Rowntree PR. 1990. A mass flux convection scheme with representation of cloud ensemble characteristics and stability-dependent closure. *Mon. Weath. Rev.* **118**: 1483–1506.
- Guichard F, Asencio N, Peugeot C, Bock O, Redelsperger J-L, Cui X, Garvert M, Lamptey B, Orlandi E, Sander J, Fierli F, Gaertner MA, Jones SC, Lafore J-P, Morse A, Nuret M, Boone A, Balsamo G, de Rosnay P, Decharme B, Harris PP, Bergès J-C. 2010. An intercomparison of simulated rainfall and evapotranspiration associated with a mesoscale convective system over West Africa. *J. Hydrometeorol.* **25**: 37–60.
- Hourdin F, Musat I, Guichard F, Ruti PM, Favot F, Filiberti M-A, Pham M, Grandpeix J-Y, Polcher J, Marquet P, Boone A, Lafore J-P, Redelsperger J-L, Dell’ aquila A, Doval TL, Traore AK, Gallée H. 2010. AMMA-model intercomparison project. *Bull. Am. Meteorol. Soc.* **91**: 95–104.
- Huffman GJ, Adler RF, Bolvin DT, Gu G, Nelkin EJ, Bowman KP, Hong Y, Stocker EF, Wolff DB. 2007. The TRMM multi-satellite precipitation analysis: Quasi-global, multi-year, combined-sensor precipitation estimates at fine scale. *J. Hydrometeorol.* **8**: 38–55.
- Janicot S, Thorncroft CD, Ali A, Asencio N, Berry G, Bock O, Bourles B, Caniaux G, Chauvin F, Deme A, Kergoat L, Lafore JP, Lavaysse C, Lebel T, Marticorena B, Mounier F, Nedelec P, Redelsperger JL, Ravegnani F, Reeves CE, Roca R, de Rosnay P, Schlager H, Sultan B, Tomasin M, Ulanovsky A, forecasters team A. 2008. Large-scale overview of the summer monsoon over West Africa during the AMMA field experiment in 2006. *Ann. Geophys.* **26**: 2569–2595.
- Klüpfel V, Kalthoff N, Gantner L, Kottmeier C. 2011a. Evaluation of soil moisture ensemble runs to estimate precipitation variability in convection permitting model simulations for West Africa. *Atmos. Res.* **101**: 178–193.
- Klüpfel V, Kalthoff N, Gantner L, Taylor C. 2011b. Convergence zones and their impact on the initiation of a mesoscale convective system in West Africa. *Q. J. R. Meteorol. Soc.* **138**: 950–963.
- Knupp KR. 2006. Observational analysis of a gust front to bore to solitary wave transition within an evolving nocturnal boundary layer. *J. Atmos. Sci.* **63**: 2016–2035.
- Koch SE, Feltz W, Fabry F, Pagowski M, Geerts B, Bedka KM, Miller DO, Wilson JW. 2008. Turbulent mixing processes in atmospheric bores and solitary waves deduced from profiling systems and numerical simulation. *Mon. Weath. Rev.* **136**: 1373–1400.
- Kohler M, Kalthoff N, Kottmeier C. 2010. The impact of soil moisture modifications on CBL characteristics in West Africa: A case-study from the AMMA campaign. *Q. J. R. Meteorol. Soc.* **136**: 442–455.
- Koster RD, Dirmeyer PA, Guo Z, Bonan G, Chan E, Cox P, Gordon CT, Kanae S, Kowalczyk E, Lawrence D, Liu P, Lu CH, Malyshev S, McAvaney B, Mitchell K, Mocko D, Oki T, Oleson K, Pitman A, Sud YC, Taylor CM, Veresghy D, Vasic R, Xue Y, Yamada T. 2004. Regions of strong coupling between soil moisture and precipitation. *Science* **305**: 1138–1140.
- Lac C, Lafore JP, Redelsperger JL. 2002. Role of gravity waves in triggering deep convection during TOGA COARE. *J. Atmos. Sci.* **59**: 1293–1316.
- Lane TP, Reeder MJ. 2001. Convectively generated gravity waves and their effect on the cloud environment. *J. Atmos. Sci.* **58**: 2427–2440.
- Lane TP, Zhang F. 2011. Coupling between gravity waves and tropical convection at mesoscale. *J. Atmos. Sci.* **68**: 2582–2598.
- Laurent H, D’Amato N, Lebel T. 1998. How important is the contribution of the mesoscale convective complexes to the Sahelian rainfall? *Phys. Chem. Earth* **23**: 629–633.
- Lin YL, Deal RL, Kulie MS. 1998. Mechanisms of cell regeneration, development, and propagation within a two-dimensional multicell storm. *J. Atmos. Sci.* **55**: 1867–1886.
- Liu C, Moncrieff MW. 2004. Effects of convectively generated gravity waves and rotation on the organization of convection. *J. Atmos. Sci.* **61**: 2218–2227.
- Lock AP, Brown AR, Bush MR, Martin GM, Smith RNB. 2000. A new boundary layer mixing scheme. Part I: scheme description and single-column model tests. *Mon. Weath. Rev.* **128**: 3187–3199.
- Lothon M, Campistron B, Chong M, Couvreux F, Guichard F, Rio C, Williams E. 2011. Life cycle of a mesoscale circular gust front observed by a C-band Doppler radar in West Africa. *Mon. Weath. Rev.* **139**: 1370–1388.
- Mapes BE. 1993. Gregarious tropical convection. *J. Atmos. Sci.* **50**: 2026–2037.
- Marsham JH, Parker DJ. 2006. Secondary initiation of multiple bands of cumulonimbus over southern Britain. II: Dynamics of secondary initiation. *Q. J. R. Meteorol. Soc.* **132**: 1053–1072.
- Mathon V, Laurent H, Lebel T. 2002. Mesoscale convective system rainfall in the Sahel. *J. Appl. Meteorol.* **41**: 1081–1092.
- Meynadier R, Bock O, Gervois S, Guichard F, Redelsperger JL, Agustí-Panareda A, Beljaars A. 2010. West African Monsoon water cycle: 2. Assessment of numerical weather prediction water budgets. *J. Geophys. Res.* **115**: D19 105. DOI:10.1029/2010JD013919.
- Morcrette C, Browning K, Blyth AM, Bozier KE, Clark PA, Ladd D, Norton EG, Pavelin E. 2006. Secondary initiation of multiple bands of cumulonimbus over southern Britain. I: An observational case-study. *Q. J. R. Meteorol. Soc.* **132**: 1021–1051.
- Mueller CK, Carbone RE. 1987. Dynamics of a thunderstorm outflow. *J. Atmos. Sci.* **44**: 1879–1898.
- Negri AJ, Adler RF, Xu L, Surratt J. 2004. The impact of Amazonian deforestation on dry season rainfall. *J. Climate* **17**: 1306–1319.
- Pellarin T, Tran T, Cohard JM, Galle S, Laurent JP, de Rosnay P, Vischel T. 2009. Soil moisture mapping over West Africa with a 30-min temporal resolution using AMSR-E observations and a satellite-based rainfall product. *Hydrol. Earth Syst. Sci.* **12**: 1887–1896.
- Pfister L, Chan KR, Bui TP, Bowen S, Legg M, Gary B, Kelly K, Proffitt M, Starr W. 1993. Gravity waves generated by a tropical cyclone during the STEP tropical field program: A case study. *J. Geophys. Res.* **98**: 8611–8638.
- Piani C, Durran D, Alexander MJ, Holton JR. 2000. A numerical study of three-dimensional gravity waves triggered by deep tropical convection and their role in the dynamics of the QBO. *J. Atmos. Sci.* **57**: 3689–3702.
- Raymond DJ. 1983. A forced gravity wave model of self-organizing convection. *J. Atmos. Sci.* **44**: 3528–3543.
- Redelsperger JL, Thorncroft CD, Diedhiou A, Lebel T, Parker DJ, Polcher J. 2006. African monsoon multidisciplinary analysis. An international research project and field campaign. *Bull. Am. Meteorol. Soc.* **87**: 1739–1746.

- Ross AN, Tompkins AM, Parker DJ. 2004. Simple models of the role of surface fluxes on convective cold pool evolution. *J. Atmos. Sci.* **61**: 1582–1595.
- Rottman JW, Simpson JE. 1989. The formation of internal bores in the atmosphere: A laboratory model. *Q. J. R. Meteorol. Soc.* **115**: 941–963.
- Segal M, Arritt RW. 1992. Nonclassical mesoscale circulations caused by surface sensible heat-flux gradients. *B. Am. Meteorol. Soc.* **73**(10): 1593–1604.
- Smith RK. 1988. Travelling waves and bores in the lower atmosphere: The ‘morning glory’ and related phenomena. *Earth-Sci. Rev.* **25**: 267–290.
- Song IS, Chun HY, Lane TP. 2003. Generation mechanisms of convectively forced internal gravity waves and their propagation to the stratosphere. *J. Atmos. Sci.* **60**: 1960–1980.
- Stensrud DJ, Fritsch JM. 1993. Mesoscale convective systems in weakly forced large-scale environments. Part I: Observations. *Mon. Weath. Rev.* **121**: 3326–3344.
- Stensrud DJ, Fritsch JM. 1994. Mesoscale convective systems in weakly forced large-scale environments. Part III: Numerical simulations and implications for operational forecasting. *Mon. Weath. Rev.* **122**: 2084–2104.
- Stobie JG, Einaudi F, Uccellini LW. 1983. A case study of gravity wave-convective storms interaction: 9 May 1979. *J. Atmos. Sci.* **40**: 2804–2830.
- Taylor CM, Clark DB. 2001. The diurnal cycle and African easterly waves: A land surface perspective. *Q. J. R. Meteorol. Soc.* **127**: 845–867.
- Taylor CM, Ellis RJ. 2006. Satellite detection of soil moisture impacts on convection at the mesoscale. *Geophys. Res. Lett.* **33**: L03404. DOI:10.1029/2005GL025252.
- Taylor CM, Lebel T. 1998. Observational evidence of persistent convective-scale rainfall patterns. *Mon. Weath. Rev.* **126**: 1597–1607.
- Taylor CM, Saïd F, Lebel T. 1997. Interactions between the land surface and mesoscale rainfall variability during HAPEX-Sahel. *Mon. Weath. Rev.* **125**: 2211–2227.
- Taylor CM, Parker DJ, Harris PP. 2007. An observational case study of mesoscale atmospheric circulations induced by soil moisture. *Geophys. Res. Lett.* **34**: L15801. DOI:10.1029/2007GL030572.
- Taylor CM, Harris PP, Parker DJ. 2010. Impact of soil moisture on the development of the Sahelian mesoscale convective system: A case-study from the AMMA Special Observing Period. *Q. J. R. Meteorol. Soc.* **136**: 456–470.
- Taylor CM, Gounou A, Guichard F, Harris PP, Ellis RJ, Coureux F, De Kauwe M. 2011. Frequency of Sahelian storm initiation enhanced over mesoscale soil-moisture patterns. *Nature Geosci.* **4**: 430–433.
- Tompkins AM. 2001. Organisation of tropical convection in low wind shears: The role of cold pools. *J. Atmos. Sci.* **58**: 1650–1672.
- Trigo IF, Monteiro IT, Olesen F, Kabcsch E. 2008. An assessment of remotely sensed land surface temperature. *J. Geophys. Res.* **113**: D17 108. DOI:10.1029/2008JD010035.
- Uccellini LW, Koch SE. 1987. The synoptic setting and possible energy sources for mesoscale wave disturbances. *Mon. Weath. Rev.* **115**: 721–729.
- Wang J, Chagnon FJF, Williams ER, Betts AK, Renno NO, Machado LAT, Bisht G, Knox R, Brase RL. 2009. Impact of deforestation in the Amazon basin on cloud climatology. *Proc. Natl. Acad. Sci.* **106**: 3670–3674.
- Wilson DR, Ballard SP. 1999. A microphysically based precipitation scheme for the UK Meteorological Office Unified Model. *Q. J. R. Meteorol. Soc.* **125**: 1607–1636.
- Wolters D, van Heerwaarden CC, Vilá-Guerau de Arellano J, Cappelaere B, Ramier D. 2010. Effects of soil moisture gradients on the path and the intensity of a West African squall line. *Q. J. R. Meteorol. Soc.* **136**: 2162–2175.
- Xue M, Xu Q, Droegeemeier KK. 1997. A theoretical and numerical study of density currents in non-constant shear flows. *J. Atmos. Sci.* **54**: 1998–2019.